UNIVERSITY OF OKLAHOMA

GRADUATE COLLEGE

ICE CRYSTAL SIZE DISTRIBUTIONS IN TROPICAL MESOSCALE CONVECTIVE SYSTEMS IN THE VICINITY OF DARWIN, AUSTRALIA: RESULTS FROM THE HAIC/HIWC CAMPAIGN

A THESIS

SUBMITTED TO THE GRADUATE FACULTY

in partial fulfillment of the requirements for the

Degree of

MASTER OF SCIENCE IN METEOROLOGY

By

PETER BRECHNER
Norman, Oklahoma
2021

Downloaded from SHAREOK. Persistent Handle URL: https://hdl.handle.net/11244/332327

ICE CRYSTAL SIZE DISTRIBUTIONS IN TROPICAL MESOSCALE CONVECTIVE SYSTEMS IN THE VICINITY OF DARWIN, AUSTRALIA: RESULTS FROM THE HAIC/HIWC CAMPAIGN

A THESIS APPROVED FOR THE
UNIVERSITY OF OKLAHOMA SCHOOL OF METEOROLOGY

BY THE COMMITTEE CONSISTING OF

Dr. Greg McFarquhar, Chair

Dr. Naoko Sakaeda

Dr. Wei Wu

© Copyright by PETER BRECHNER 2021
All Rights Reserved.

Contents

Abstract v
1. Introduction 1
2. HAIC/HIWC Data 4
3. Results 6
   a. Modality Fraction 8
   b. Means and Plausible Ranges of Parameters 12
4. Conclusion and Discussion 21
   a. Multimodality in SDs 21
   b. SD parameters 23
   c. HIWC conditions 25
Appendix A – Methodology for Finding Multiple Modes in Distributions 27
Tables and Figures 33
References 50

Abstract

Total ice water content (IWC) derived from an isokinetic evaporator probe and ice crystal size distributions measured by a two-dimensional stereo probe and precipitation imaging probe installed on the French Falcon aircraft during the collaborative European High Altitude Ice Crystals – North American High IWC field campaign (HAIC-HIWC) based out of Darwin, Australia in 2014 are used to characterize high IWC regions (areas with IWC greater than 1.5 g m^{-3} and median mass dimension (MMD) less than 0.5 mm, hereafter HIWC regions; areas with IWC greater than 1.5 g m^{-3} with any MMD are hereafter high IWC regions). A fitting routing that automatically determines whether a unimodal, bimodal, or trimodal gamma distribution best fits an observed size distribution was developed and used to determine the characteristics of the size distributions (e.g., presence of unimodal/bimodal/trimodal distributions, fit parameters characterized by volume of equally realizable parameters to account for variability and uncertainty, etc.). The variation of these characteristics and bulk properties (median mass diameter, IWC) were determined as a function of temperature, IWC, and vertical velocity. HIWC regions were most pronounced in updraft cores. The three modes of the size distribution give information on different processes contributing to ice growth: nucleation for crystals with maximum dimension $D < 150$ μm, diffusion (150 μm $< D <$ 1000 μm), and aggregation ($D >$ 1000 μm). The occurrence frequency of trimodal distributions increased with temperature. The volumes of equally plausible parameters derived in the phase space of gamma fit parameters increased with temperature for unimodal distributions. For multimodal distributions, the volumes increased with temperature for temperatures less than −27°C. Bimodal distributions with a

nucleation mode were most common in updraft cores and HIWC regions, whereas bimodal distributions with an aggregation mode were least common in updraft and downdraft cores.

1. Introduction

In recent years, some aircraft have experienced engine events or ice accumulations in pitot tubes when flying in the vicinity of convection in regions with radar reflectivity less than 20 dBZ (e.g., Lawson et al. 1998; Mason et al. 2006; Bravin et al. 2015). Since supercooled water during such events has mainly been absent (Mason et al. 2006), these regions are likely dominated by high ice water contents contained mainly in small ice crystals. Given the potential commercial aircraft hazard, the multi-agency High-Altitude Ice Crystals/High Ice Water Content (HAIC/HIWC) field campaign was organized (Dezitter et al. 2013; Strapp et al. 2016a). The first phase was based out of Darwin, Australia in January and February 2014 with the purpose to better characterize the statistical properties of cloud particles in such regions. As a consequence, particle size distributions, bulk properties, and environmental conditions in regions of mesoscale convective systems with high ice water content (HIWC) were measured. These data considerably extended data collected in tropical cirrus outflows and convection from prior experiments that either did not focus on regions close to convective cores where IWCs are typically higher (e.g., McFarquhar and Heymsfield 1996; Heymsfield et al. 2002; Bouniol et al. 2010; Diao et al. 2013), potentially underestimated IWCs because of saturation of common bulk probes in high IWC environments (Davison et al. 2016; Strapp et al. 2016b), or that estimated IWCs from observed SDs without a reference bulk mass content (e.g. Heymsfield et al. 2004; Lawson et al. 2010; Fontaine et al. 2014).

These data expand data from previous studies that have shown HIWC regions dominated by large numbers of small ice crystals indeed exist. For example, Fridlind et al. (2015) used in-situ measurements obtained by Airbus to show that HIWC regions had median area-equivalent

diameters of 200 to 300 μm. Leroy et al. (2017) found that ice crystals from 250 to 500 μm dominated the mass size distribution in most MCSs using the HAIC/HIWC data, suggesting that smaller size crystals dominate both the mass and area size distributions. However, in two MCSs, Leroy et al. (2017) conversely found that ice crystals from 400 to 800 μm dominated the mass size distribution. Thus, the meteorological context of the observations must be examined to determine what conditions are conducive to the occurrence of HIWCs dominated by small ice crystals.

To aid in process understanding and for use in numerical model and remote sensing parameterization schemes, observed particle size distributions (PSDs) are typically fit to analytic functions such as gamma functions (e.g. Dudhia 1989; Kosarev and Mazin 1991; Mitchell 1991; Rotstayn 1997; Reisner et al. 1998; Gilmore et al. 2004; Ferrier 1994; Walko et al. 1995; Meyers et al. 1997; Straka and Mansell 2005; Milbrandt and Yau 2005; McFarquhar et al. 2015; Jackson et al. 2015; Leroy et al. 2017), lognormal functions (McFarquhar and Heymsfield 1997), power law functions (Heymsfield and Platt 1984), and exponential functions (McFarquhar and Black 2004). Parameterizations using gamma functions, represented by

$$\mathrm{N}(D) = N_0 D^{\mu} \exp(-\lambda D), \tag{1.1}$$

where D is the maximum ice crystal dimension, λ is the slope, μ is the shape parameter, and N_0 the intercept, require information about how the fit parameters vary with environmental conditions for their application. Power law and exponential functions are special cases of gamma functions with $\lambda = 0$ and $\mu = 0$, respectively. Figure 1 visualizes how the values of N_0, μ, and λ affect the shape of a PSD. It is seen that increasing N_0 increases the number distribution function N(D) of all sized particles equally. Increasing μ reduces the N(D) of particles with small D more

than those with large D, increasing the median particle size. Increasing λ reduces the N(D) of particles with large D more than those with small D, decreasing the median particle size. Properties of the PSD, such as total number concentration N_t, extinction β, ice water content IWC, mass-weighted terminal velocity v_m, and effective radius R_e, can be determined by integrating the gamma function, since it is easily integrable.

Although gamma distributions have been frequently found to well characterize some ice crystal PSDs since 1963 (Borovikov et al. 1963), in some instances they do not well represent the observations. In such cases, a sum of different functions is needed to characterize the PSD as shown for studies of rain (Willis 1984; McFarquhar and List 1991) and of ice crystals (McFarquhar and Heymsfield 1997). Recently, Jackson et al. (2015) showed that ice crystal PSDs observed over the United States Southern Great Plains can be bimodal, with peaks in $N(D)$ occurring at D of around 50 and 300 μm under some conditions. Since a single gamma distribution function cannot characterize a bimodal distribution, Jackson et al. (2015) represented each mode as a gamma distribution, determining the parameters of each mode by extending McFarquhar et al. (2015)'s fitting technique to represent each mode using a separate incomplete gamma distribution. In this study, this technique is extended further to parameterize PSDs as sums of up to three complete gamma distributions. Further, an enhancement makes the new technique easier to implement in models: each mode is fit so that it covers all possible sizes of ice crystals, rather than having separate modes represent only specific parts of the PSD as assumed by Jackson et al. (2015). This permits easier implementation in models. Gamma distributions are assumed in model parameterization schemes such as the Weather Research and Forecasting (WRF) Single-Moment 6-class (WSM6) and WRF Double-Moment 6-class (WDM6) schemes (Morrison et al. 2009).

This paper uses data obtained from the first HAIC/HIWC campaign conducted in the vicinity of Darwin, Australia to examine how the characteristics of PSDs vary with environmental conditions such as temperature and vertical velocity and microphysical properties such as ice water content and median mass diameter. The remainder of the paper is organized as follows. Section 2 describes the instruments used and conditions sampled during HAIC/HIWC, as well as the methodology used to process the data. Key results of this paper are shown in section 3 and summarized in section 4. Section 4 also offers direction for future work.

2. HAIC/HIWC Data

The First Phase of the HAIC/HIWC campaign was based out of Darwin, Australia between 16 January and 18 February 2014. Instruments were installed on the French Falcon aircraft to measure ice crystal properties in-situ, with flights conducted primarily at four different temperature levels (−53°C to −43°C, hereafter $T_{43\text{-}53}$; −43°C to −33°C ($T_{33\text{-}43}$); −33°C to −21°C ($T_{21\text{-}33}$); and −5°C to −21°C ($T_{5\text{-}21}$)) in order to get statistics to better characterize the HIWC environment. The PSDs of ice crystals were measured using a two-dimensional stereo (2DS) probe and a precipitation imaging probe (PIP). The 2DS probe has a pair of orthogonal laser beams which cross in the center of the sample volume. These beams illuminate two linear 128-photodiode arrays, each of which has a resolution of 10 μm (Lawson et al. 2006), so that the 2DS probe nominally measures particles with D between 10 μm and 1.28 mm. To process the data for the HAIC-HIWC project, the two photodiode arrays were treated as separate arrays, and the PSDs from the horizontal and vertical arrays were averaged to create a PSD.

The PIP probe has 64 photodiodes and a photodiode resolution of 100 μm. Thus, it nominally measures particles with D between 100 μm and 6.4 mm. Following Leroy et al. (2017), an integrated size distribution was constructed by using the 2DS data for D smaller than 0.8 mm, the PIP data for D larger than 1.2 mm, and for $0.8 < D < 1.2$ mm, a weighted average of the size distributions from each instrument according to

$$\mathrm{N}(D) = \mathrm{W}_{\mathrm{2DS}}(D)\,\mathrm{N}_{\mathrm{2DS}}(D) + \mathrm{W}_{\mathrm{PIP}}(D)\,\mathrm{N}_{\mathrm{PIP}}(D), \tag{2.1}$$

where

$$\mathrm{W}_{\mathrm{2DS}}(D) = \frac{1.2\mathrm{mm} - D}{1.2\mathrm{mm} - 0.8\mathrm{mm}} \tag{2.2}$$

and

$$\mathrm{W}_{\mathrm{PIP}}(D) = \frac{D - 0.8\mathrm{mm}}{1.2\mathrm{mm} - 0.8\mathrm{mm}} \tag{2.3}$$

Due to the reduction in the depth of field of the 2DS for small D and the potential impact of shattered particles (Field et al. 2003, 2006), only particles with $D > 50$ μm were used to determine N(D). Corrections were made for out of focus particles (Korolev 2007) and shattered particles (Field et al. 2003, 2006), and particle reconstruction was used to extend the size range of measured particles following Heymsfield and Parrish (1979).

While uncertainties in relationships between environmental conditions and microphysical properties are typically dominated by the variability in PSDs (e.g., McFarquhar et al. 2015; Finlon et al. 2019), knowledge of statistical sampling errors is important for the automatic algorithm developed here to classify distributions as having one, two, or three modes. Each 5-second averaged PSD is classified as unimodal, bimodal, or trimodal according to the smallest

number of modes that can be used to fit the distribution within the statistical uncertainty of the measured PSD. Even if an observed PSD can be described by a multi-modal distribution, it would still be represented as a unimodal distribution if it was adequately characterized by such within the statistical sampling error. Appendix A describes the algorithm developed to determine the number of modes as well as to determine the parameters describing each gamma function.

An isokinetic evaporator (IKP2) probe measured the ice water content (IWC) for all cloud penetrations, providing unique data near the convective cores in HIWC conditions (Davison et al., 2016; Strapp et al., 2016b). The IKP2 probe was designed to make measurements up to at least 10 g m^{-3} at 200 m s^{-1} with 20 percent target accuracy (Davison et al. 2008). Development of the IKP2 probe and uncertainties in total water content (TWC) measurements are described in Davison et al. (2016) and Strapp et al. (2016b). Processes used to subtract supercooled liquid water from the TWC measurements are described in Leroy et al. (2017).

A multi-beam 95GHz Doppler cloud radar (Radar SysTem Airborne, RASTA) provided vertical velocity measurements (Protat et al., 2009; Leroy et al., 2016). A deiced Rosemount sensor was used to measure air temperature.

3. Results

SDs measured during the HAIC/HIWC field campaign were fit to sums of one to three gamma distributions using the methodology approach described in Section 2 and developed in more detail in Appendix A. Frequencies of occurrence of different types of distributions

(unimodal, bimodal1, bimodal2, trimodal) are discussed in Section 3a while most likely gamma fit parameters and their plausible ranges are discussed in Section 3b.

Examples of SDs for each type of distribution (unimodal, bimodal1, bimodal2, trimodal) identified using the methodology described in Appendix A are shown in figure 2 with the unimodal and, if applicable, multimodal fit. Bimodal1 and bimodal2 are differentiated by D_{cutoff}, the value of D where N(D) from each mode is equal. Values of D_{cutoff} are clustered around 0.15 mm and 1.0 mm. Bimodal1 distributions have $D_{\text{cutoff}} \approx 0.15$ mm, while bimodal2 distributions have $D_{\text{cutoff}} \approx 1.0$ mm. The use of up to three modes to characterize size distributions was found to reduce fitting errors in estimates of bulk parameters such as Z and MMD, as shown in Table 1. The mean fitting error in Z for unimodal distributions was −0.04 dB (−0.9%), with a standard deviation of 0.22 dB (5.0%). For bimodal1 distributions, the mean fitting error was −0.01 dB (−0.1%) for a bimodal fit and −0.08 dB (−1.9%) for a unimodal fit, with standard deviations of 0.12 dB (2.8%) for a bimodal fit and 0.74 dB (17%) for a unimodal fit. For bimodal2 distributions, the mean fitting error was −0.13 dB (−2.9%) for a bimodal fit and −0.66 dB (−14%) for a unimodal fit, with standard deviations of 0.22 dB (5.1%) and 0.99 dB (23%) respectively. For trimodal distributions, the mean fitting error was −0.06 dB (−1.4%) for a trimodal fit and −0.25 dB (−5.6%) for a unimodal fit, with standard deviations of 0.19 dB (4.4%) and 1.40 dB (32%) respectively. The mean fitting error in MMD for unimodal distributions was 32 μm (7.1%), with a standard deviation of 31 μm (7.0%). The mean fitting error in MMD for bimodal1 distributions was 27 μm (5.1%) for bimodal fits as opposed to 9 μm (1.6%) for unimodal fits, with standard deviations of 25 μm (4.8%) and 44 μm (8.3%), respectively. The mean fitting error in MMD for bimodal2 distributions was −2 μm (−0.3%) for bimodal fits versus 92 μm (13%) for unimodal fits, with standard deviations of 17 μm (2.3%) and 110 μm

(15%), respectively. Finally, the mean fitting error in MMD for trimodal distributions was 8 μm (1.5%) for trimodal fits against 99 μm (19%) for unimodal fits, with standard deviations of 14 μm (2.7%) and 90 μm (17%) respectively. In general, the errors in fitting the moments for the unimodal distribution are lower when it is one of the moments that was minimized in the fitting procedure. In this study, the difference between the 0^{th}, 2^{nd}, and 4^{th} moments between the observed and fit distributions were minimized. Thus, the mean percentage errors in IWC for the unimodal fits were smaller and less dependent on modality compared to those for *Z* or MMD because IWC is roughly proportional to the second moment, which is the middle moment used in fitting gamma distributions. The high percentage errors in *Z*, which is roughly proportional to the fourth moment, and MMD, which is roughly proportional to the ratio between the third and second moments, for unimodal fits compared to the errors for bimodal2 and trimodal distributions show the importance of the large *D* mode in affecting the third and fourth moments and their related quantities like MMD and *Z*.

a. Modality Fraction

Figure 4 shows how the fractions of observed PSDs classified as unimodal, bimodal1, bimodal2, and trimodal vary as a function of *T*. For $T_{43\text{-}53}$, 48% of distributions were unimodal, 10% bimodal1, 41% bimodal2, and 1% trimodal. For $T_{33\text{-}43}$, 36% of distributions were unimodal, 17% bimodal1, 43% bimodal2, and 5% were trimodal. For $T_{21\text{-}33}$, 28% of distributions were unimodal, 15% bimodal1, 42% bimodal2, and 15% trimodal. For $T_{5\text{-}21}$, 16% of distributions were unimodal, 11% bimodal1, 52% bimodal2, and 21% trimodal.

The relationship, illustrated in Figure 4, between *T* and occurrence of different types of multimodal distributions, shows that a large crystal mode centered at *D* around 2 mm (present in bimodal2 and trimodal distributions) is more common at higher *T* near −13°C (73%) compared

to lower T near −48°C (42%) and that its fractional importance monotonically increases with increasing temperature. This trend is consistent with the aggregation of smaller particles as they fall in the anvil producing the large mode. Further evidence of aggregation is illustrated in Figure 5, which shows the presence of many aggregates and irregular particles in images of particles with 4 mm < D < 6 mm from 3:34:33 UTC to 3:34:38 UTC on 8 February 2014, when the bimodal2 PSD in Figure 2c was observed. A small crystal mode centered at D around 0.08 mm (present in bimodal1 and trimodal distributions) is also more common at T near −13°C (32%) compared to T near −48°C (11%). This is consistent with findings from previous studies (e.g., Zhao et al. 2010; Jackson et al. 2015) that showed bimodal conditions with $D \approx 0.1$ mm separating modes were more common at higher T. The previous studies hypothesized that bimodality, and by extension the small crystal mode, results from heterogeneous nucleation in the presence of sedimentation. Although there has been some concern that the presence of the smaller crystal mode may be associated with the correction factors applied for out of focus particles, the fact that the peak does not always occur and has variable height suggests that its presence is indeed caused by the variability in the concentration of the smaller ice crystals. Considering that the rate of heterogeneous nucleation decreases with T (e.g., Cooper 1986; Morrison and Gettelman 2008), more research on PSDs for D < 0.1 mm is warranted for stronger understanding of ice microphysics at these maximum dimensions, including stronger understanding of what may cause the small D mode to increase in frequency with T. One possibility is that as T increases, aggregation of crystals with D < 0.1 mm increases, resulting in a peak in N(D) near D = 0.3 mm in addition to the peak in N(D) near or below D = 0.05 mm that is observed at all ranges of T. If this is the case, the small D mode may represent heterogeneous

nucleation in PSDs where aggregation of small ice crystals increases the shape parameter of the medium *D* mode.

Figure 6 shows how the fraction of observed PSDs classified as unimodal, bimodal1, bimodal2, and trimodal change as a function of vertical velocity (*w*). The fraction of observed PSDs classified as unimodal changed from 49% of PSDs for downdrafts to 29% of PSDs for stratiform to 40% of PSDs for updrafts. The fraction of observed PSDs classified as bimodal1 changed from 22% of PSDs for downdrafts to 11% of PSDs for stratiform to 31% of PSDs for updrafts. The fraction of observed PSDs classified as bimodal2 changed from 26% of PSDs for downdrafts to 52% of PSDs for stratiform to 17% of PSDs for updrafts. The fraction of observed PSDs classified as trimodal changed from 4% for downdrafts to 9% for stratiform to 12% for updrafts.

The small crystal mode occurs more frequently in updrafts (43%) than in downdrafts (26%) or stratiform conditions (20%), consistent with heterogeneous nucleation occurring in updrafts. This is further evidence that the small crystal mode is real rather than an instrument artifact. Conversely, a large crystal mode occurs more frequently in stratiform conditions (61%) than in updrafts (30%) or downdrafts (29%). When particles are detrained from convective updrafts, they can aggregate and grow in the stratiform regions behind the updrafts (e.g., McFarquhar et al. 2007). The smaller vertical velocities in stratiform conditions also allow particles in these conditions more time to grow and accumulate.

Figure 7 shows how the fractions of observed PSDs classified as unimodal, bimodal1, bimodal2, and trimodal change as a function of IWC. The fraction of unimodal distributions grows from 30% for IWC < 1.0 g m^{-3} to 50% for IWC ≈ 1.6 g m^{-3} before decreasing to 21% for IWC ≈ 2.7 g m^{-3}. The fraction of bimodal1 distributions grows from 12% for IWC < 1.0 g m^{-3} to

22% for IWC ≈ 1.6 g m^{-3} to 52% for IWC ≈ 2.7 g m^{-3}. The fraction of bimodal2 distributions drops from 50% for IWC < 1.0 g m^{-3} to 20% at IWC ≈ 1.6 g m^{-3} to 1% at IWC ≈ 2.7 g m^{-3}. The fraction of trimodal distributions grows from 8% for IWC < 1.0 g m^{-3} to 9% for IWC ≈ 1.6 g m^{-3} to 25% for IWC ≈ 2.7 g m^{-3}.

The small crystal mode occurs most frequently at IWC ≈ 2.7 g m^{-3} (77%, compared to 31% for IWC ≈ 1.6 g m^{-3} and 20% for IWC < 1.0 g m^{-3}). Conversely, a large crystal mode occurs most frequently at IWC < 1.0 g m^{-3} (58%, compared to 29% for IWC ≈ 1.6 g m^{-3} and 26% for IWC ≈ 2.7 g m^{-3}). The fact that the small crystal mode is occurring more frequently for the higher IWCs is indicative that clouds with large IWCs and large amounts of small ice crystals were indeed sampled during the HAIC/HIWC Darwin campaign, and hence these data can be used to develop representations of what the SDs look like in these conditions. The relationship between IWC and modality type seems to parallel the relationship between vertical velocity and modality type, with higher IWC having modality fractions near those for updrafts and lower IWC having modality fractions near those for stratiform. Figure 8 confirms that IWC is higher in updrafts with $w \geq 1.0$ m s^{-1} (1.2 g m^{-3}) and downdrafts with $w \leq -1.0$ m s^{-1} (1.0 g m^{-3}) than in stratiform regions with -0.2 m $s^{-1} \leq w \leq 0.2$ m s^{-1} (0.6 g m^{-3}). The relationship between vertical velocity and IWC forms a V-shape with a minimum somewhere in -0.2 m $s^{-1} \leq w \leq 0.0$ m s^{-1}. Figure 9 shows that HIWC conditions were observed more frequently in updrafts (37%) and downdrafts (32%) than in stratiform regions (9%). While this can be inferred from Figure 8 for all regions with high IWC, Figure 9 shows that this applies even with the added constraint of MMD < 0.5 mm.

Figure 10 shows how the fraction of observed PSDs classified as unimodal, bimodal1, bimodal2, and trimodal change as a function of MMD. The fraction of unimodal distributions

decreases from 65% for MMD < 0.4 mm to 7% for MMD ≥ 0.7 mm. As the aggregation of small ice crystals in bimodal1 PSDs occurs mainly at higher *T*, at which PSDs tend to have large MMD, most PSDs with small MMD have neither a small crystal mode nor a large crystal mode and therefore are unimodal. The fraction of bimodal1 distributions averages 17% for MMD < 0.4 mm and 16% for 0.4 mm ≤ MMD < 0.7 mm, decreasing for MMD ≥ 0.7 mm to 1% for MMD ≥ 1.5 mm. The fraction of bimodal2 distributions increases from 10% for MMD < 0.4 mm to 79% for MMD ≥ 0.7 mm, consistent with the largest MMDs resulting from aggregation of smaller crystals. The fraction of trimodal distributions averages 8% for MMD < 0.4 mm, 11% for 0.4 mm ≤ MMD < 0.7 mm, and 5% for MMD ≥ 0.7 mm. In HIWC conditions, 52% of PSDs are unimodal, 28% are bimodal1, 7% are bimodal2, and 13% are trimodal. The high percentage of unimodal PSDs and relatively high percentage of bimodal1 PSDs are consistent with the high IWC, high *w*, and small MMD that characterize these conditions. A better characterization of these multimodal PSDs in HIWC and other conditions is needed for development of improved parameterizations for cloud resolving models that would more accurately represent microphysical processes occurring in such conditions. The next Section examines how the multimodal gamma distributions can be characterized in such conditions.

b. Means and Plausible Ranges of Parameters

To develop parameterizations of HIWC and other conditions, it is important to know the values of the parameters describing the gamma distributions as well as the modality of the distributions. As discussed in Section 2, the approach of McFarquhar et al. (2015) is followed to give ranges of fit parameters describing the gamma distributions to represent the uncertainty and variability in such parameters. Volumes of equally realizable solutions are computed using the covariance matrices and form spaces enclosing all points less than 3.368 standard deviations

from the most likely solution. The factor of 3.368 was chosen because the chi-squared test with 3 degrees of freedom has a p-value of 0.01 at 3.368^2, ensuring a 99% probability that a random solution will fall within the enclosed space. Figure 11 shows the plausible range of gamma fit parameters for unimodal distributions characterizing all conditions, conditions with MMD < 0.5 mm, and conditions when HIWCs are present (i.e., MMD < 0.5 mm and IWC > 1.5 g m^{-3}). The maximum values of all the parameters are seen to increase with temperature in Figure 11. The plausible range of parameters is smaller for unimodal distributions in HIWC conditions than for unimodal conditions in general. The mean values of μ and N_0 increase with temperature while the mean value of λ shows little dependence on temperature. However, as these trends are hard to visualize in three-dimensional volume plots, projections of these volumes are examined in two-dimensional phase space of the different fit parameters, as shown in figure 12, to more clearly show these trends. To more easily see how the most likely (N_0,μ,λ) and three-dimensional ellipsoids of equally realizable solutions vary with T, projections are shown in two-dimensional $\log_{10}(N_0)$–μ (Fig. 12a-d), $\log_{10}(N_0)$–λ (Fig. 12e-h), and μ-λ (Fig. 12i-l) phase space.

It should also be noted that parts of the ellipses where $\mu \leq -1$ or $\lambda \leq 0$ describing the equally realizable solutions at all temperatures are not physically plausible when the distributions cover the complete range of particle sizes. These parts of the ellipses are cutoff and not shown in Fig. 12. Although such values are realistic for incomplete gamma distributions that cover a finite range of particle sizes, they are unrealistic as $\mu \leq -1$ and $\lambda \leq 0$ both mean that the zeroth moment of the complete gamma distribution is not integrable, and $\lambda < 0$ would give an exponential increase in number distribution function with D, which does not occur in nature.

Figure 12 compares the most likely and plausible range of gamma fit parameters for unimodal distributions in all conditions, conditions with MMD < 0.5 mm, and conditions when

HIWCs are present (i.e., MMD < 0.5 mm and IWC > 1.5 g m^{-3}) for four ranges of *T*. Figure 13 compares the most likely and plausible range of gamma fit parameters for distributions identified as unimodal (red) to the most likely and plausible range of gamma fit parameters for unimodal fits to all distributions regardless of whether they were identified as unimodal, bimodal1, bimodal2, or trimodal (blue). Figure 14 compares the most likely and plausible range of gamma fit parameters for particles characterized by the mode with smaller maximum dimensions (red) to the most likely and plausible range of gamma fit parameters for particles characterized by the mode with larger maximum dimensions (blue) in bimodal1 distributions. For biomdal2 distributions, Figure 15 compares the most likely and plausible range of gamma fit parameters for the gamma distribution characterizing particles with a smaller peak maximum dimension (red) to those for the gamma distribution characterizing particles with a larger peak maximum dimension (blue). Figure 16 compares the most likely and plausible range of gamma fit parameters for particles characterized by the modes with smaller maximum dimensions (red), medium maximum dimensions (green), and larger maximum dimensions (blue).

Figures 12a-d show that for unimodal distributions in all conditions, the most likely value of μ increases with *T* from -0.3 for $T_{43\text{-}53}$ to 2.1 for $T_{5\text{-}21}$, while the most likely value of N_0 increases with *T* from $10^{8.9}$ m^{-4} $cm^{-\mu}$ for $T_{43\text{-}53}$ to $10^{11.8}$ m^{-4} $cm^{-\mu}$ for $T_{5\text{-}21}$. For small-MMD conditions, the most likely value of μ increases with *T* from -0.3 for $T_{43\text{-}53}$ to 2.6 for $T_{5\text{-}21}$, while the most likely value of N_0 increases with *T* from $10^{9.0}$ m^{-4} $cm^{-\mu}$ for $T_{43\text{-}53}$ to $10^{13.5}$ m^{-4} $cm^{-\mu}$ for $T_{5\text{-}21}$. For HIWC conditions, the most likely value of μ increases with *T* from -0.4 for $T_{43\text{-}53}$ to 0.9 for $T_{5\text{-}21}$, while the most likely value of N_0 increases with *T* from $10^{9.5}$ m^{-4} $cm^{-\mu}$ for $T_{43\text{-}53}$ to $10^{11.3}$ m^{-4} $cm^{-\mu}$ for $T_{5\text{-}21}$. The red ellipses show an increase in the variances in $\log_{10}(N_0)$ and μ with *T* for unimodal distributions in all conditions with the volumes of the ellipsoids in the three-

dimensional ($\log_{10}(N_0)$,μ,λ) phase space ranging from 41 mm^{-1} at $T_{43\text{-}53}$ to 330 mm^{-1} at $T_{5\text{-}21}$. The green ellipses show an increase in the variances in $\log_{10}(N_0)$ and μ with T for small-MMD conditions with the volumes of the ellipsoids in the three-dimensional ($\log_{10}(N_0)$,μ,λ) phase space ranging from 39 mm^{-1} at $T_{43\text{-}53}$ to 250 mm^{-1} at $T_{5\text{-}21}$. The blue ellipses show a weak increase in the variances in $\log_{10}(N_0)$ and μ with T for HIWC conditions with the volumes of the ellipsoids in the three-dimensional ($\log_{10}(N_0)$,μ,λ) phase space ranging from 1.5 mm^{-1} at $T_{43\text{-}53}$ to 7.0 mm^{-1} at $T_{21\text{-}33}$.

Figures 12e-h show how the plausible range of N_0 and λ change with T, and figures 12i-l show how the plausible range of μ and λ change with T. For unimodal distributions in all conditions, the most likely λ increases with T from 6.1 mm^{-1} for $T_{43\text{-}53}$ to 7.7 mm^{-1} for $T_{5\text{-}21}$. For small-MMD conditions, the most likely λ increases with T from 6.4 mm^{-1} for $T_{43\text{-}53}$ to 12 mm^{-1} for $T_{5\text{-}21}$. For HIWC conditions, the most likely λ shows no relationship with T with values ranging from 6.3 mm^{-1} for $T_{33\text{-}43}$ to 7.7 mm^{-1} for $T_{5\text{-}21}$.

There is less variability in the gamma distribution parameters that describe unimodal PSDs in HIWC conditions than there is in the gamma distribution parameters that describe unimodal PSDs in other conditions. There is less change with T in the gamma distribution parameters that describe unimodal PSDs in HIWC conditions as well. The most likely values of μ that describe unimodal PSDs in HIWC conditions are small, ranging from −0.4 to 0.9. Considering most PSDs in HIWC conditions are unimodal, in some models, it may suffice to model PSDs in HIWC conditions using a fixed exponential distribution.

Figures 13a-d show that for unimodal fits to all distributions, the most likely value of μ increases with T from −0.5 for $T_{43\text{-}53}$ to 0.6 for $T_{21\text{-}33}$ before dropping to 0.5 for $T_{5\text{-}21}$, while the most likely value of N_0 increases with T from $10^{8.5}$ m^{-4} cm$^{-\mu}$ for $T_{43\text{-}53}$ to $10^{9.7}$ m^{-4} cm$^{-\mu}$ for $T_{21\text{-}33}$

before dropping to $10^{9.1}$ m^{-4} $cm^{-\mu}$ for $T_{5\text{-}21}$. For unimodal fits to unimodal distributions, the most likely value of μ increases monotonically with T from −0.3 for $T_{43\text{-}53}$ to 2.1 for $T_{5\text{-}21}$, with a value of 1.0 for $T_{21\text{-}33}$, while the most likely value of N_0 also increases monotonically with T from $10^{8.9}$ m^{-4} $cm^{-\mu}$ for $T_{43\text{-}53}$ to $10^{11.8}$ m^{-4} $cm^{-\mu}$ for $T_{5\text{-}21}$, with a value of $10^{10.7}$ m^{-4} $cm^{-\mu}$ for $T_{21\text{-}33}$. The blue ellipses show an increase in the variances in $\log_{10}(N_0)$ and μ with T for the unimodal fits to all distributions with the volumes of the ellipsoids in the three-dimensional ($\log_{10}(N_0)$,μ,λ) phase space ranging from 32 mm^{-1} at $T_{43\text{-}53}$ to 190 mm^{-1} at $T_{5\text{-}21}$. With a volume of 150 mm^{-1} at $T_{21\text{-}33}$, the volume increases most steeply at the lowest temperatures. The red ellipses also show an increase in the variances in $\log_{10}(N_0)$ and μ with T for the unimodal fits to unimodal distributions with the volumes of the ellipsoids in the three-dimensional ($\log_{10}(N_0)$,μ,λ) phase space ranging from 41 mm^{-1} at $T_{43\text{-}53}$ to 330 mm^{-1} at $T_{5\text{-}21}$. With a volume of 130 mm^{-1} at $T_{21\text{-}33}$, the volume increases most steeply at higher temperatures.

Figures 13e-h show how the plausible range of N_0 and λ change with T, and figures 13i-l show how the plausible range of μ and λ change with T. For all distributions, the most likely λ increases with T from 5.1 mm^{-1} for $T_{43\text{-}53}$ to 5.6 mm^{-1} for $T_{21\text{-}33}$ before dropping to 4.3 mm^{-1} for $T_{5\text{-}21}$, while for unimodal distributions, λ increases monotonically with T from 6.1 mm^{-1} for $T_{43\text{-}53}$ to 7.7 mm^{-1} for $T_{5\text{-}21}$, with a value of 7.3 mm^{-1} for $T_{21\text{-}33}$. Since aggregates are more prevalent in the multimodal distributions as shown in Figure 5, the decrease in λ between $T_{21\text{-}33}$ and $T_{5\text{-}21}$ and the smaller increase in λ between $T_{43\text{-}53}$ and $T_{21\text{-}33}$ for all distributions are associated with the presence of larger aggregates in the multimodal distributions included in the unimodal fits to all distributions. The presence of larger aggregates in multimodal distributions also explains why N_0 and μ decrease between $T_{21\text{-}33}$ and $T_{5\text{-}21}$ for all distributions and why the rate of increase in the variances of N_0, μ, and λ slows with T for all distributions – larger aggregates increase the

median mass dimension, decreasing λ; the greater separation in maximum dimension between the largest aggregates and other crystals decreases μ and λ; and the strong positive codependence between N_0, μ, and λ decreases N_0.

The blue and red ellipses overlap less at high T compared to low T with the overlap fraction for $\log_{10}(N_0)-\mu$ being 81% at $T_{43\text{-}53}$ compared to 55% at $T_{5\text{-}21}$., the overlap fraction for $\log_{10}(N_0)-\lambda$ being 78% at $T_{43\text{-}53}$ compared to 57% at $T_{5\text{-}21}$, and the overlap fraction for $\mu-\lambda$ being 79% at $T_{43\text{-}53}$ compared to 53% at $T_{5\text{-}21}$. This is consistent with a larger fraction of multimodal distributions occurring at high T as shown in Fig. 4, and the presence of aggregates at high T as shown in Fig. 5. Comparing the most likely (N_0,μ,λ) for the true unimodal distributions against those obtained for unimodal fits to all distributions shows that ($\log_{10}(N_0)$,μ,λ) are (0.4,0.2,1.0 mm^{-1}) greater for $T_{43\text{-}53}$, but the differences increase to (2.7,1.6,3.4 mm^{-1}) at $T_{5\text{-}21}$. The smaller values for the unimodal fits to all distributions is associated with the presence of larger aggregates in the large mode of the distribution. The difference in fit parameters between true unimodal distributions and unimodal distributions fit to all distributions at higher temperatures, combined with the reduced overlap between ellipses describing the equally realizable solutions at the higher temperatures, shows that although unimodal fits produce an adequate representation of the size distributions at lower temperatures, the same is not likely true at the higher temperatures.

Figures 14a-d show that for particles with larger maximum dimension, the most likely value of μ increases with T from 1.2 for $T_{43\text{-}53}$ to 3.3 for $T_{5\text{-}21}$, while the most likely value of N_0 increases with T from $10^{12.2}$ m^{-4} $cm^{-\mu}$ for $T_{43\text{-}53}$ to $10^{13.8}$ m^{-4} $cm^{-\mu}$ for $T_{5\text{-}21}$. For particles with smaller maximum dimension, the most likely value of μ increases with T from 0.6 for $T_{43\text{-}53}$ to 1.1 for $T_{5\text{-}21}$ while the most likely value of N_0 has no dependence on T with values between $10^{11.9}$

m^{-4} $cm^{-\mu}$ and $10^{12.2}$ m^{-4} $cm^{-\mu}$ for all T. The blue ellipses show an increase in the variances in $\log_{10}(N_0)$ and μ with T for particles with larger maximum dimension with the volumes of the ellipsoids in the three-dimensional ($\log_{10}(N_0)$,μ,λ) phase space ranging from 26 mm^{-1} at $T_{43\text{-}53}$ to 270 mm^{-1} at $T_{5\text{-}21}$. The red ellipses also show an increase in the variances in $\log_{10}(N_0)$ and μ with T for particles with smaller maximum dimension with the volumes of the ellipsoids in the three-dimensional ($\log_{10}(N_0)$,μ,λ) phase space ranging from 510 mm^{-1} at $T_{43\text{-}53}$ to 4000 mm^{-1} at $T_{5\text{-}21}$.

Figures 14e-h show how the plausible range of N_0 and λ change with T, and figures 14i-l show how the plausible range of μ and λ change with T. For particles with larger maximum dimension, the most likely λ stays the same with T, ranging from 9.0 mm^{-1} for $T_{5\text{-}21}$ to 11 mm^{-1} for $T_{21\text{-}33}$. For particles with smaller maximum dimension, the most likely λ increases with T from 40 mm^{-1} for $T_{43\text{-}53}$ to 67 mm^{-1} for $T_{5\text{-}21}$.

Overlap between the blue and red ellipses depends little on T with the overlap fraction for $\log_{10}(N_0)$–μ being 24.5% at $T_{43\text{-}53}$ compared to 29.6% at $T_{5\text{-}21}$, the overlap fraction for $\log_{10}(N_0)$–λ being 3.96% at $T_{43\text{-}53}$ compared to 3.28% at $T_{5\text{-}21}$, and the overlap fraction for μ–λ being 4.77% at $T_{43\text{-}53}$ compared to 5.49% at $T_{5\text{-}21}$.

Figures 15a-d show that for particles with larger maximum dimensions, the most likely value of μ increases slightly with T from 1.3 for $T_{43\text{-}53}$ to 1.9 for $T_{5\text{-}21}$, while the most likely value of N_0 varies little with T, ranging between $10^{9.2}$ m^{-4} $cm^{-\mu}$ for $T_{21\text{-}33}$ and $10^{9.7}$ m^{-4} $cm^{-\mu}$ for $T_{33\text{-}43}$. For particles characterized by the smaller peak, the most likely value of μ increases with T from 0.3 for $T_{43\text{-}53}$ to 1.8 for $T_{5\text{-}21}$ while the most likely value of N_0 also increases with T from $10^{9.9}$ m^{-4} $cm^{-\mu}$ for $T_{43\text{-}53}$ to $10^{11.8}$ m^{-4} $cm^{-\mu}$ for $T_{5\text{-}21}$. The blue ellipses show a small increase in the variances in $\log_{10}(N_0)$ and μ with T for particles characterized by the larger peak with the volumes of the ellipsoids in the three-dimensional ($\log_{10}(N_0)$,μ,λ) phase space ranging from 28

mm^{-1} at $T_{43\text{-}53}$ to 41 mm^{-1} at $T_{5\text{-}21}$. The red ellipses show a larger increase in the variances in $\log_{10}(N_0)$ and μ with T for particles in the smaller peak with the volumes of the ellipsoids in the three-dimensional ($\log_{10}(N_0)$,μ,λ) phase space ranging from 19 mm^{-1} at $T_{43\text{-}53}$ to 100 mm^{-1} at $T_{5\text{-}21}$.

Figures 15e-h show how the plausible range of N_0 and λ change with T, and figures 15i-l show how the plausible range of μ and λ change with T. For particles characterized by the larger peak, the most likely λ decreases with T from 3.7 mm^{-1} for $T_{43\text{-}53}$ to 2.6 mm^{-1} for $T_{5\text{-}21}$. For particles in the smaller peak, the most likely λ varies little with T, increasing from 8.3 mm^{-1} for $T_{43\text{-}53}$ to 9.5 mm^{-1} for $T_{33\text{-}43}$, before decreasing back to 8.3 mm^{-1} for $T_{5\text{-}21}$. Since particles with larger maximum dimensions in bimodal2 distributions tend to be aggregates, as shown in Figure 5, the decrease in λ with T for the larger peak is associated with the maximum dimension of the largest aggregates increasing with temperature.

The blue and red ellipses overlap more at high T compared to low T with the overlap fraction for $\log_{10}(N_0)$–μ being 9.1% at $T_{43\text{-}53}$ compared to 10.1% at $T_{5\text{-}21}$, the overlap fraction for $\log_{10}(N_0)$–λ being 10.3% at $T_{43\text{-}53}$ compared to 20.1% at $T_{5\text{-}21}$, and the overlap fraction for μ–λ being 7.6% at $T_{43\text{-}53}$ compared to 14.5% at $T_{5\text{-}21}$. This is related to the increase in the fraction of the volume of the ellipsoid for the smaller peak with $\lambda \leq 0$ with T. As T increases, the shape of the mode for the smaller peak becomes less consistent between SDs at the same T, with the mode sometimes representing clusters of particles with approximately the same maximum dimension and other times representing particles with widely varying maximum dimension. Where the mode for the smaller peak represents the latter, it can have gamma parameters close to those for the mode characterizing the larger peak.

Figures 16a-d show that for particles with smaller maximum dimension, the most likely value of μ stays the same with T, ranging from 0.9 for $T_{43\text{-}53}$ to 1.2 for $T_{33\text{-}43}$, while the most likely value of N_0 decreases with T from $10^{13.6}$ m^{-4} $cm^{-\mu}$ for $T_{43\text{-}53}$ to $10^{12.2}$ m^{-4} $cm^{-\mu}$ for $T_{5\text{-}21}$. For particles with medium maximum dimension, the most likely value of μ increases with T from 2.0 for $T_{43\text{-}53}$ to 4.9 for $T_{5\text{-}21}$, while the most likely value of N_0 increases with T from $10^{14.1}$ m^{-4} $cm^{-\mu}$ for $T_{43\text{-}53}$ to $10^{17.8}$ m^{-4} $cm^{-\mu}$ for $T_{5\text{-}21}$. For particles with larger maximum dimension, the most likely value of μ increases with T from 2.8 for $T_{43\text{-}53}$ to 5.1 for $T_{5\text{-}21}$, while the most likely value of N_0 increases with T from $10^{11.5}$ m^{-4} $cm^{-\mu}$ for $T_{43\text{-}53}$ to $10^{14.2}$ m^{-4} $cm^{-\mu}$ for $T_{5\text{-}21}$. The red ellipses show an increase in the variances in $\log_{10}(N_0)$ and μ with T for particles with smaller maximum dimension with the volumes of the ellipsoids in the three-dimensional $(\log_{10}(N_0),\mu,\lambda)$ phase space ranging from 390 mm^{-1} at $T_{43\text{-}53}$ to 1800 mm^{-1} at $T_{5\text{-}21}$. The green ellipses show an increase in the variances in $\log_{10}(N_0)$ and μ with T for particles with medium maximum dimension with the volumes of the ellipsoids in the three-dimensional $(\log_{10}(N_0),\mu,\lambda)$ phase space ranging from 110 mm^{-1} at $T_{43\text{-}53}$ to 400 mm^{-1} at $T_{5\text{-}21}$. The blue ellipses show an increase in the variances in $\log_{10}(N_0)$ and μ with T for particles with larger maximum dimension with the volumes of the ellipsoids in the three-dimensional $(\log_{10}(N_0),\mu,\lambda)$ phase space ranging from 27 mm^{-1} at $T_{43\text{-}53}$ to 110 mm^{-1} at $T_{5\text{-}21}$.

Figures 16e-h show how the plausible range of N_0 and λ change with T, and figures 16i-l show how the plausible range of μ and λ change with T. For particles with smaller maximum dimension, the most likely λ stays the same with T, ranging from 52 mm^{-1} for $T_{43\text{-}53}$ to 67 mm^{-1} for $T_{21\text{-}33}$. For particles with medium maximum dimension, the most likely λ stays the same with T, ranging from 16 mm^{-1} for $T_{43\text{-}53}$ to 18 mm^{-1} for $T_{21\text{-}33}$. For particles with larger maximum

dimension, the most likely λ stays the same with T, ranging from 5.3 mm^{-1} for $T_{43\text{-}53}$ to 7.5 mm^{-1} for $T_{21\text{-}33}$.

4. Conclusion and Discussion

Multiple occurrences of HIWC regions in areas of low reflectivity have previously been observed over tropical oceans, suggesting large concentrations of small ice crystals are present. The causes of these large concentrations of small ice crystals are poorly known. The HAIC-HIWC field campaign was conducted to research the environmental and meteorological conditions and microphysical processes associated with HIWC regions. Insight into these conditions is gained through comparison of this study with prior studies, examining how the use of a new fitting technique yields information on multimodal SDs in Section 4a, hypothesizing how environmental and microphysical conditions and processes affect gamma fit parameters in Section 4b, and discussing environmental and microphysical conditions and processes present in HIWC regions are discussed in Section 4c.

a. Multimodality in SDs

Ice crystal PSDs in HIWC and other regions were fit to unimodal and multimodal gamma distributions to aid in process understanding and to develop parameterizations for use in remote sensing and numerical modeling schemes. Since some PSDs cannot be represented well by gamma distributions, a method of representing observed PSDs as sums of gamma functions that is compatible with parameterization schemes used in current modeling and remote sensing schemes was developed. The fitting technique developed by McFarquhar et al. (2015) was

extended to parameterize PSDs as sums of up to three complete gamma distributions. The use of three gamma distributions allows more precise fitting of the data as shown in Table 1 and Fig. 2. The large mode characterizing particles with *D* greater than 1 mm was not identified in previous studies examining multimodal PSDs (e.g., Zhao et al. 2010, Jackson et al. 2015) because it is not typically associated with a distinct peak in number distribution function. Thus, the gamma functions characterizing this mode cannot be directly compared against distributions from previous studies. However, the identification and inclusion of the large mode in the multimodal distributions was shown in Table 1 to increase the accuracy and precision of fit-derived estimates of *Z* and MMD more than the identification and inclusion of the small mode characterizing particles with *D* less than 0.1 mm. Analysis of the properties of multimodal distributions and how the likelihood of a distribution being bimodal1, bimodal2, or trimodal varies with environmental and microphysical conditions provides insight into what processes occur in HIWC regions and other regions of tropical MCSs.

The prevalence of unimodal, bimodal, and trimodal distributions is a function of environmental conditions such as temperature, vertical velocity, and ice water content, as well as of microphysical conditions such as median mass diameter. The likelihood of a small mode increases with *T* (Fig. 4), with $|w|$ (Fig. 6), and with IWC (Fig. 7) which itself increases with $|w|$ (Fig. 8). The increase in the likelihood of a small mode with *T* was also observed by Jackson et al. (2015) and Zhao et al. (2010), with the latter hypothesizing that this was caused by heterogeneous nucleation in the presence of sedimentation. The large mode is most common in stratiform regions of convective outflow (Fig. 6), and its likelihood increases with temperature (Fig. 4) and MMD (Fig. 10), suggesting the large mode results from aggregation of smaller particles as illustrated in Fig. 5. Aggregation of smaller particles is known to increase with *T* for

$T < -15$°C (Connolly et al. 2012), and the change in likelihood of small D and large D modes with T is consistent with the presence of aggregation of small D and medium D particles (Fig. 4). As the difference in saturation vapor pressure over water and ice increases, the diffusional growth rate increases (e.g., Hoffmann 2020). However, the likelihood of a PSD being unimodal decreases with T, suggesting that a single gamma distribution may fit ice particles that form from homogeneous nucleation, heterogeneous nucleation, or diffusional growth wherever aggregation is lacking.

b. SD parameters

The use of up to three gamma distributions to characterize size distributions affects the most likely values of N_0, μ, and λ for PSDs fit to a single gamma distribution, as well as the dependence of these most likely values on environmental conditions. For unimodal PSDs, the scale parameter N_0, shape parameter μ, and slope parameter λ all increase with T, with μ decreasing with IWC. While an increase in μ with T was also found in Jackson et al. (2015), that study found a decrease in λ and no change in N_0 with T. Not only could varying PSDs associated with differences in meteorological conditions sampled cause this difference, but also the recognition of a large D mode in the multimodal distributions identified could limit the number of unimodal distributions with large MMD. When all PSDs in this study are fit using a single mode, λ decreases with T at warmer T in agreement with Jackson et al. (2015) (Fig. 13), showing that the large D mode does indeed decrease λ in single mode gamma fits. This is expected because the presence of the large mode increases the sizes of the largest ice particles in the PSD.

In this study, volumes of equally realizable solutions are computed using the covariance matrices and form spaces enclosing all points less than 3.368 standard deviations from the most likely solution. The factor of 3.368 was chosen because the chi-squared test with 3 degrees of

freedom has a p-value of 0.01 at 3.368^2, ensuring a 99% probability that a random solution will fall within the enclosed space. Previous studies (e.g., Jackson et al. 2015) constructed volumes of equally realizable solutions using the methodology described in McFarquhar et al. (2015), which considers all possible solutions with moments between their minimum and maximum estimates and typically produces larger volumes than those produced using covariance matrices for individual PSDs, though not necessarily for families or large sets of PSDs. Solutions in Jackson et al. (2015), which analyzed data acquired in stratiform regions behind mid-latitude MCSs with T < −20°C, had N_0 ranging from 10^9 and 10^{19} m^{-4} $cm^{-\mu}$, μ ranging from −2 to 4 (Jackson et al. 2015 allowed $-2 < \mu$), and λ ranging from 0.1 to 100 mm^{-1}, while solutions in this study over a similar range of temperatures have N_0 ranging from $10^{3.5}$ and $10^{17.9}$ m^{-4} $cm^{-\mu}$, μ ranging from −1.0 to 5.1, and λ ranging from 0.0 to 18 mm^{-1}. Compared to the Jackson et al. (2015) study, this study has significantly lower values of λ, suggesting large crystals were more common in the HAIC/HIWC dataset than in the SPARTICUS dataset.

Typical averages and ranges of N_0, μ, and λ for each mode in multimodal distributions were computed. For the small mode, μ does not vary with temperature. In the presence but not in the absence of the large mode, N_0 decreases with temperature. In the absence but not in the presence of the large mode, λ increases with temperature. The standard deviations of N_0 and μ increase with temperature. For the large mode, N_0 and μ are independent of temperature while λ decreases with temperature. The standard deviations of N_0 and λ increase with temperature when a significant small mode is absent. For the medium mode, N_0 and μ increase with temperature while λ is independent of temperature. The standard deviations of $N0$, μ, and λ all increase with temperature. The average value of μ for the medium mode is higher when a significant small mode is present than when a significant small mode is absent.

The procedure used for fitting multimodal distributions assumes that μ and λ are no larger and smaller, respectively, for the small mode and no smaller and larger, respectively, for the large mode than for the medium mode. While this ensures that large D bins have minimal effect on small mode parameters and small D bins have minimal effect on large mode parameters when optimizing fits, the assumption may not always be true. For example, the assumption may be violated for μ between the medium and large modes in trimodal distributions at temperatures warmer than −40°C some unknown fraction of the time that increases with T. In PSDs where the assumption is violated, the true mean value of μ_2 may exceed 5 at temperatures warmer than −40°C while the true mean value of μ_3 may be closer to the true mean value of μ_2 for bimodal2 distributions. Since the fitting procedure underestimates μ_2 and overestimates μ_3 when $\mu_3 < \mu_2$, this limitation of the fitting procedure must be considered when analyzing the relationship of each mode's parameters with temperature and other environmental conditions.

c. HIWC conditions

As updraft and downdraft strength increase, IWC increases, making high ice mass more likely (Fig. 8). Indeed, PSDs with high ice masses and small median mass dimensions are more common in updrafts and downdrafts than in stratiform regions (Fig. 9). These findings are consistent with the locations of reports of high IWC. "Extremely high IWC (1 g m^{-3}) near the convection" was reported in McFarquhar and Heymsfield (1996), while during spiral descents performed in convectively generated cirrus anvils, Heymsfield et al. (2004) documented "exceptionally large IWCs of nearly 1 g m^{-3}…near the tops of the layers" (Leroy et al. 2017).

Compared to PSDs in other regions with high ice mass, PSDs in HIWC regions are less likely to have a small mode. This may be due to MMD increasing with aggregation of small ice particles and to a single mode well representing the smaller ice crystals where aggregation of

small ice particles is lacking. Compared to PSDs in conditions with IWC < 1.5 g m^{-3}, PSDs in HIWC regions are more likely to have a small mode and less likely to have a large mode. This is consistent with the reflectivity values of Z < 30 dBZ observed in HIWC regions.

This study examined the nature of PSDs in HIWC conditions, extending knowledge learned from data collected in prior experiments in tropical cirrus outflows and convection. Previous experiments and studies either did not focus on regions close to convective cores where IWCs are typically higher (e.g., McFarquhar and Heymsfield 1996; Heymsfield et al. 2002; Bouniol et al. 2010; Diao et al. 2013), potentially underestimated IWCs because of saturation of common bulk probes in high IWC environments (Davison et al. 2016; Strapp et al. 2016b), or estimated IWCs from observed SDs without a reference bulk mass content (e.g. Heymsfield et al. 2004; Lawson et al. 2010; Fontaine et al. 2014), leaving scientists and pilots without an understanding of how high IWC can get in regions close to convective cores with Z < 30 dBZ or of what causes HIWC conditions to occur. This study revealed that PSDs in HIWC conditions have high concentrations of small ice crystals, with IWC > 1.5 g m^{-3} and MMD < 0.5 mm, with these HIWC conditions occurring in updrafts and downdrafts near convective cores where accumulation of small ice crystals is minimal.

More research is necessary to reduce uncertainty in number concentration at small crystal sizes and study links between multimodality, PSD fit parameters, microphysical properties such as ice crystal habits, and other environmental conditions such as aerosol amount and strength of, age of, and proximity to convection. Also, the results of this study apply only to conditions measured off the coast of Darwin and represent a very limited set of data, so more data in HIWC conditions is necessary to determine how representative conditions measured during HAIC/HIWC Darwin are.

Appendix A – Methodology for Finding Multiple Modes in Distributions

Previous algorithms used to represent an observed size distribution as a single gamma function (McFarquhar et al. 2015) or as the sum of two gamma functions (Jackson et al. 2015) were modified in order to represent a size distribution as the sum of up to three gamma functions. Rather than using an incomplete gamma function as in the previous studies, a complete gamma function was used to that the parameterization can be more easily implemented in a model. Further, each gamma function in a sum was evaluated from 0 to infinity, rather than evaluating the modes over a limited size range with a cutoff between them as in Jackson et al. (2015).

Many PSDs observed in Darwin have shoulders, meaning that for some range of D, N(D) decreases less steeply than would be predicted by a single gamma distribution best matching the observed shape. Some PSDs also exhibit distinct peaks, as observed by Jackson et al. (2015). Thus, even though the observed and fit moments are matched well using the incomplete gamma fit (IGF) routine of McFarquhar et al. (2015), the IGF fit distribution still overestimates N(D) for certain sizes, making it necessary to represent shoulders and peaks in size distributions using separate gamma modes for a more precise fit.

The new methodology represents PSDs as sums of up to three gamma distributions – a small mode to represent the peaks at $D < 0.2$ mm observed by Jackson et al. (2015), a medium mode to represent shoulders or peaks at 0.2 mm $< D <$ 1.0 mm, close to the median mass diameter, and a large mode to represent shoulders or peaks at $D > 1.0$ mm. The fitting methodology used here requires information about the statistical uncertainty in the measured

N(*D*), which following McFarquhar and Heymsfield (1997) and McFarquhar et al. (2015) is assumed to be equal to the square root of the number of crystals counted in a size bin over the averaging time interval (5 s here) divided by the probe sample volume and bin width. Since the size distributions measured by the 2DS and PIP probes were processed and combined into one distribution before being made available for this research, the raw counts of ice crystals used to calculate the statistical error was estimated using the processed distributions and knowledge of the sample volumes of each instrument.

For a feature in an observed PSD to be represented as a separate mode, three criteria need to be met: 1) it must be possible to fit all modes precisely from 0 to infinity; 2) the mode must represent a peak or shoulder; and 3) the mode must have a distinct shape. To determine whether each criterion is met, a test is performed. Each test returns a significance *s* for its criterion. Note that *s* is not the probability that a peak or shoulder exists, but rather a measure of how pronounced a possible peak or shoulder appears to be with respect to the criterion tested. The criterion is met if the significance returned by the test exceeds a predefined significance threshold. The significance threshold used here is 0.4. A smaller significance threshold would result in more trimodal fits, while a larger significance threshold would result in more unimodal fits. The threshold of 0.4 used here ensures that the set of distributions classified as bimodal or trimodal would be representative for conditions producing the most distinct modes in size distributions.

Thresholds of 0.333 and 0.5 were also tested. At a threshold of 0.333, only about 20% of distributions were classified as unimodal as opposed to 33% when using a threshold of 0.4. Further, little difference existed between median multimodal distributions and median unimodal distributions, especially for small *D*. At a threshold of 0.5, only about 14% of distributions were

classified as having a small mode (trimodal or bimodal small), and only about 4% of distributions were classified as trimodal as opposed to 24% of distributions having a small mode and 9% being trimodal for a threshold of 0.4. About 51% of distributions were classified as unimodal at a threshold of 0.5. However, at a threshold of 0.4, noticeable differences exist between median multimodal distributions and median unimodal distributions.

The tests, which assume the presence of the medium mode and check for the presence of a small or large mode with $s \geq 0.4$, are performed assuming D_{cutoff}, the unknown diameter where N(D) from the medium mode is equal to N(D) from the small or large mode. D_{cutoff} is a member of a set of arbitrary predefined values. When testing for the presence of a small mode, tests are performed in descending order assuming

$$D_{cutoff} = \{0.20, 0.19, 0.18, 0.17, 0.16, 0.15, 0.14, 0.13, 0.12, 0.11, 0.10, 0.09, 0.08\} \text{ mm.}$$

When testing for the presence of a large mode, tests are performed in ascending order assuming

$$D_{cutoff} = \{0.5, 0.6, 0.7, 0.8, 0.9, 1.0, 1.1, 1.2, 1.3, 1.4, 1.5, 1.6, 1.7\} \text{ mm.}$$

Testing is done for the large mode first, then for the small mode, then a second time for the large mode. The tests are as follows:

- For the small mode,
    - If tests for the large mode revealed a large mode with $s \geq 0.4$ from all three tests exists, let D_l be the value of D_{cutoff} maximizing the large mode's s from the third test. Otherwise, let $D_l = \infty$.
    - Fit the observed N(D) for $D_{cutoff} < D < D_l$ to a unimodal gamma fit, hereafter represented as $\mathrm{N}_{\mathrm{fit_1}}(D)$, using the IGF routine of McFarquhar et al (2015).

- Fit the observed N(D) for $D < D_l$ to a unimodal gamma fit, hereafter represented as $\mathrm{N}_{\mathrm{fit_2}}(D)$, using the IGF routine of McFarquhar et al (2015).
- Test for criterion #1: The observed N(D) for $D < D_{cutoff}$ exceeds by a factor of at least $\frac{s}{1-s}$ that predicted by extrapolating $\mathrm{N}_{\mathrm{fit_1}}(D)$ with 95 percent probability, as determined using a chi-squared test.
- Test for criterion #2: The ratio between the first and zeroth moments of the observed N(D) for $D < D_{cutoff}$ is less than $\sqrt{1-s}$ times that predicted by extrapolating $\mathrm{N}_{\mathrm{fit_1}}(D)$ with 95 percent probability.
- Test for criterion #3: Denote the observed number concentration with $\frac{D_{cutoff}(1+a_1)}{2a_1} \le D \le \frac{D_{cutoff}(1+a_1)}{2}$ as *B*, the observed number concentration with $D < \frac{D_{cutoff}(1+a_1)}{2a_1}$ as *A*, and the observed number concentration with $D > \frac{D_{cutoff}(1+a_1)}{2}$ as *C*, where $a_1 = \frac{0.5mm}{D_{cutoff}}$. (The arbitrary value a_1 is an estimate of the ratio $\frac{\lambda_s}{\lambda_m}$, where λ_m is the unknown slope for the medium mode and λ_s is the unknown slope for the small mode.) The value of $\frac{AC}{B^2}$ exceeds by a factor of at least $\frac{s}{1-s}$ what it would be if the data perfectly fit $\mathrm{N}_{\mathrm{fit_2}}(D)$ with 95 percent probability.

- For the large mode,

- If tests for the small mode revealed a small mode with $s \geq 0.4$ from all three tests exists, let D_s be the value of D_{cutoff} maximizing the small mode's s from the third test. Otherwise, let $D_s = 0$.
- Fit the observed N(D) for $D_s < D < D_{cutoff}$ to a unimodal gamma fit, hereafter represented as $\mathrm{N}_{\mathrm{fit_3}}(D)$, using the IGF routine of McFarquhar et al (2015).
- Fit the observed N(D) for $D > D_s$ to a unimodal gamma fit, hereafter represented as $\mathrm{N}_{\mathrm{fit_4}}(D)$, using the IGF routine of McFarquhar et al (2015).
- Test for criterion #1: The observed N(D) for $D > D_{cutoff}$ exceeds by a factor of at least $\frac{s}{1-s}$ that predicted by extrapolating $\mathrm{N}_{\mathrm{fit_3}}(D)$ with 95 percent probability.
- Test for criterion #2: The ratio between the third and second moments of the observed N(D) for $D > D_{cutoff}$ is greater than $\sqrt{\frac{1}{1-s}}$ times that predicted by extrapolating $\mathrm{N}_{\mathrm{fit_3}}(D)$ with 95 percent probability.
- Test for criterion #3: Denote the observed number concentration with $\frac{D_{cutoff}(1+a_2)}{2} \leq D \leq \frac{D_{cutoff}(1+a_2)}{2a_2}$ as *B*, the observed number concentration with $D < \frac{D_{cutoff}(1+a_2)}{2}$ as *A*, and the observed number concentration with $D > \frac{D_{cutoff}(1+a_2)}{2a_2}$ as *C*, where $a_2 = 0.4$. (The arbitrary value a_2 is an estimate of the ratio $\frac{\lambda_l}{\lambda_m}$, where λ_m is the unknown slope for the medium mode and λ_l is the

unknown slope for the large mode.) The value of $\frac{AC}{B^2}$ exceeds by a factor of at least $\frac{s}{1-s}$ what it would be if the data perfectly fit $\mathrm{N}_{\mathrm{fit_4}}(D)$ with 95 percent probability.

For both small and large modes, the mode is established if all three tests are passed for some D_{cutoff}. If all three tests are passed at multiple values of D_{cutoff}, the value of D_{cutoff} maximizing *s* from the third test is assumed to be the true cutoff diameter until the final multimodal fit is produced.

Tables and Figures

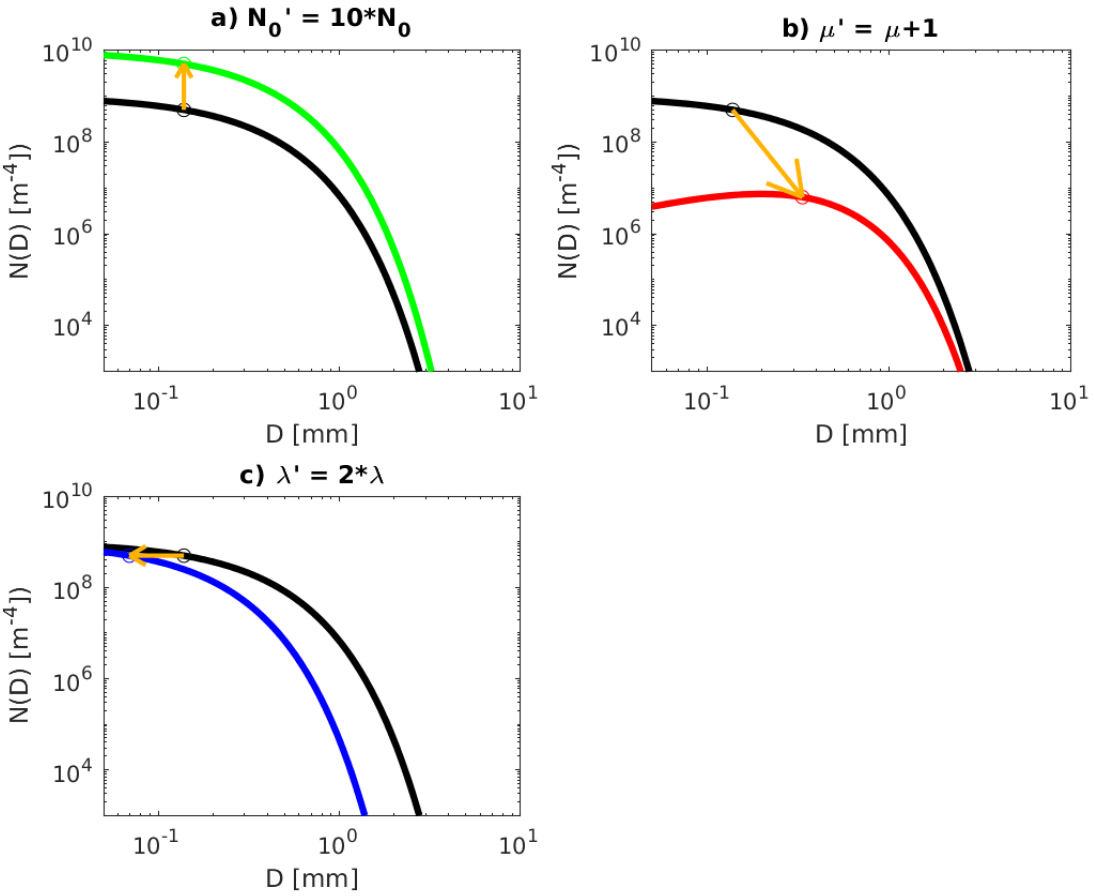


Figure 1: Illustration of how change in a) N_0, b) μ, and c) λ affect N(D). Base unimodal gamma distribution represented by black line corresponds to $N_0 = 10^9$ m^{-4} cm$^{-\mu}$, $\mu = 0$, and $\lambda = 5$ mm^{-1}. a) green line shows gamma function with $N_0' = 10*N_0$. b) red line shows gamma function with $\mu' = \mu+1$. c) blue line shows gamma function with $\lambda' = 2*\lambda$. Gold arrows show change in median diameter for change in gamma distribution.

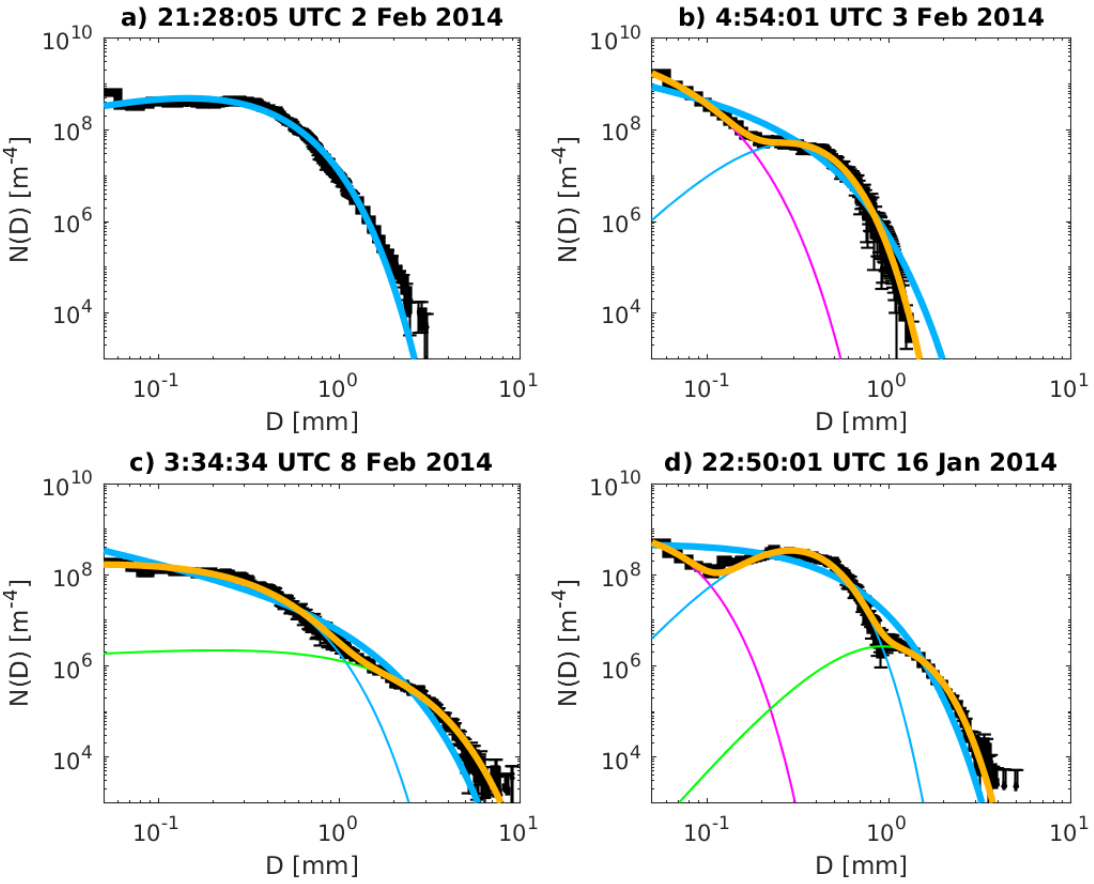


Figure 2: N(*D*) versus *D* for PSDs measured at a) 21:28:05 UTC on 2 Feb 2014 representing unimodal distribution, b) 4:54:01 UTC on 3 Feb 2014 representing bimodal1 distribution, c) 3:34:34 UTC on 8 Feb 2014 representing bimodal2 distribution, and a) 22:50:01 UTC on 16 Jan 2014 representing trimodal distribution. Fits to small modes plotted in magenta, medium modes in thin light blue, and large modes in green. Sums of modes representing multimodal fits plotted in gold, and best unimodal fits to each observed PSD plotted in thick light blue. Observed N(*D*) plotted in thick black, with error bars plotted in thin black corresponding to statistical uncertainty in observed N(*D*).

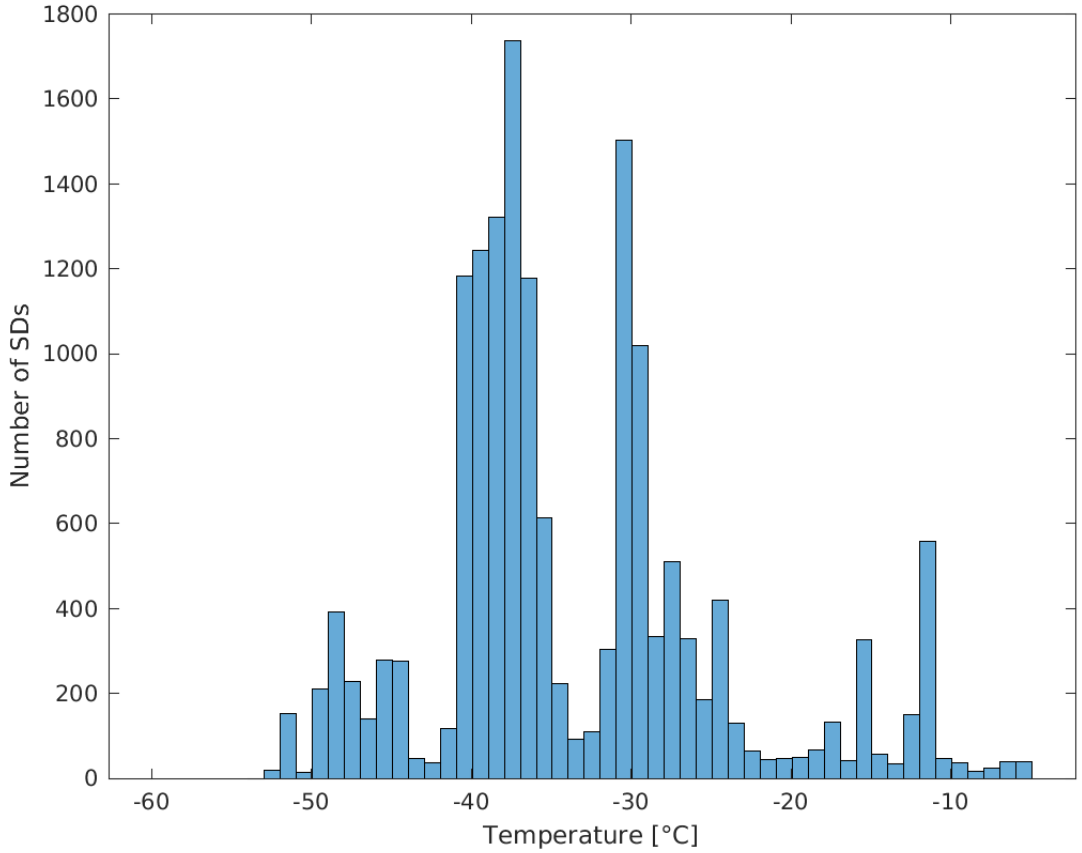


Figure 3: Histogram of observed PSDs at each temperature between -60°C and -5°C. Peaks in the histogram are observed near the four temperature levels flown at: -48°C, -38°C, -27°C, and -13°C.

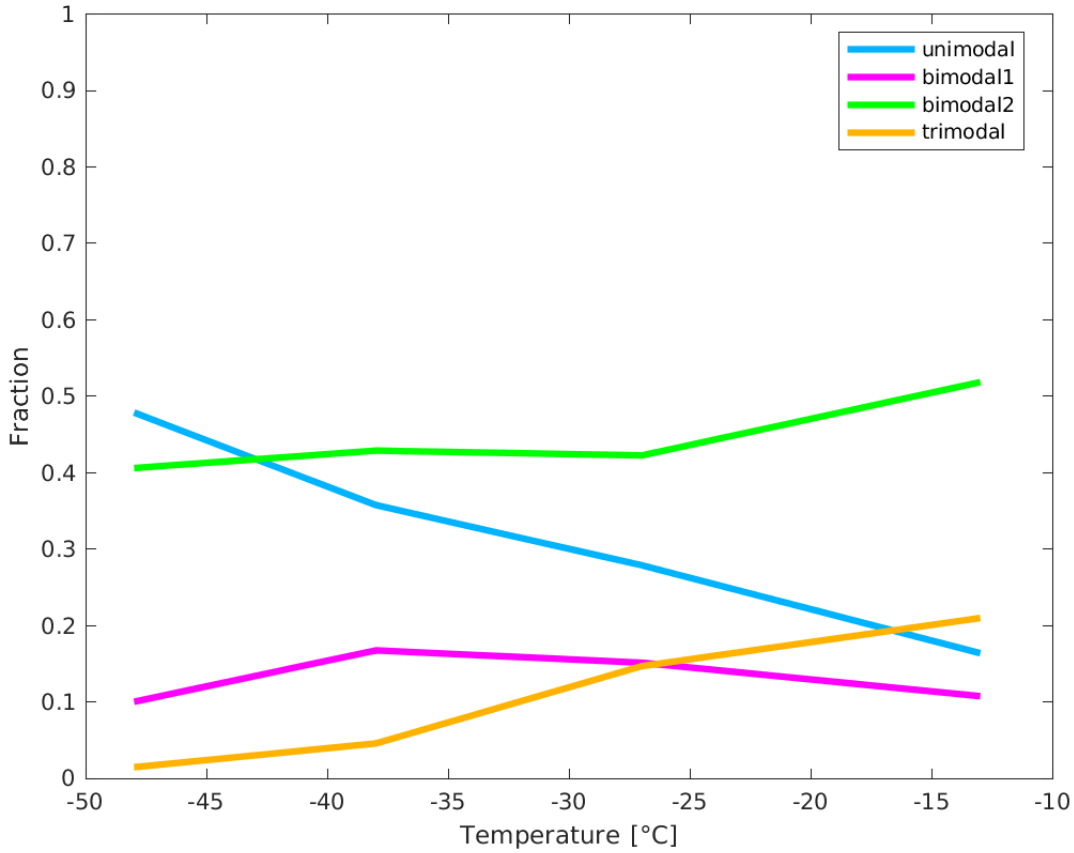


Figure 4: Fraction of observed PSDs classified as unimodal (light blue), bimodal1 (magenta), bimodal2 (green), and trimodal (gold) as a function of temperature.

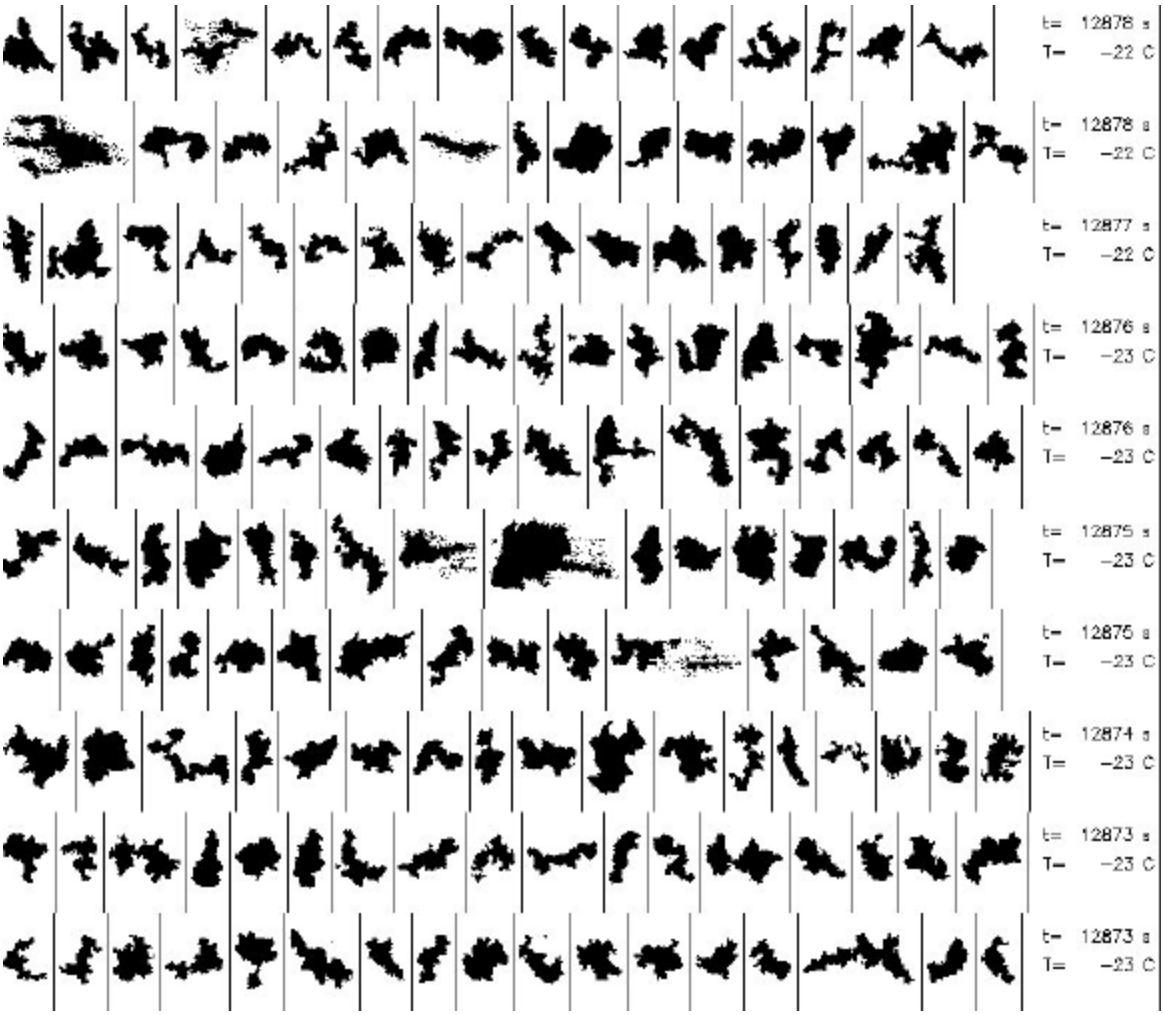


Figure 5: Selected images of ice crystals with sizes between 4 and 6 mm from 3:34:33 UTC to 3:34:38 UTC on 8 Feb 2014. (Image copyright University Corporation for Atmospheric Research.)

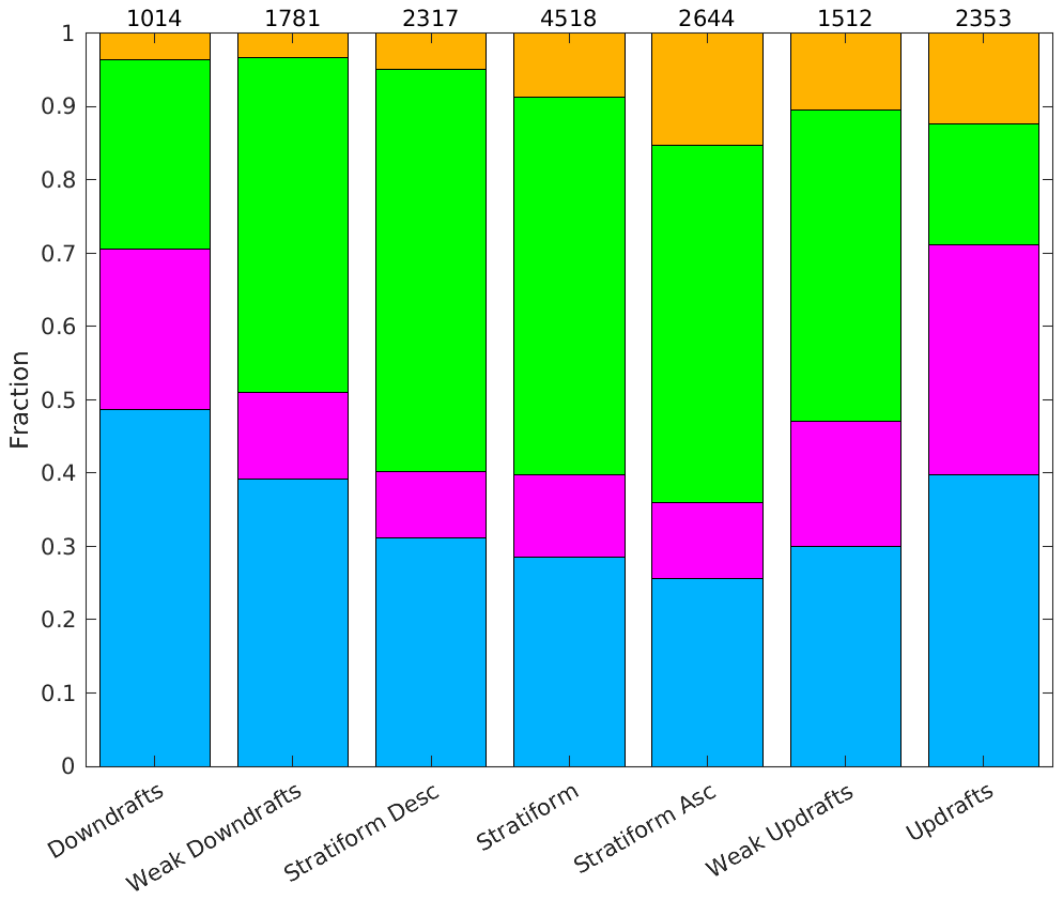


Figure 6: Fraction of observed PSDs classified as unimodal (light blue), bimodal1 (magenta), bimodal2 (green), and trimodal (gold) as a function of vertical velocity. "Downdrafts" are regions where $w \leq -1$ m s^{-1}. "Weak Downdrafts" are regions where -1 m s^{-1} $< w \leq -0.5$ m s^{-1}. "Stratiform Desc" refers to regions where -0.5 m s^{-1} $< w \leq -0.2$ m s^{-1}. "Stratiform" refers to regions where -0.2 m s^{-1} $< w < 0.2$ m s^{-1}. "Stratiform Asc" refers to regions where 0.2 m s^{-1} $\leq w < 0.5$ m s^{-1}. "Weak Updrafts" are regions where 0.5 m s^{-1} $\leq w < 1$ m s^{-1}. "Updrafts" are regions where $w \geq 1$ m s^{-1}. Sample sizes for each region are indicated at the top of each bar.

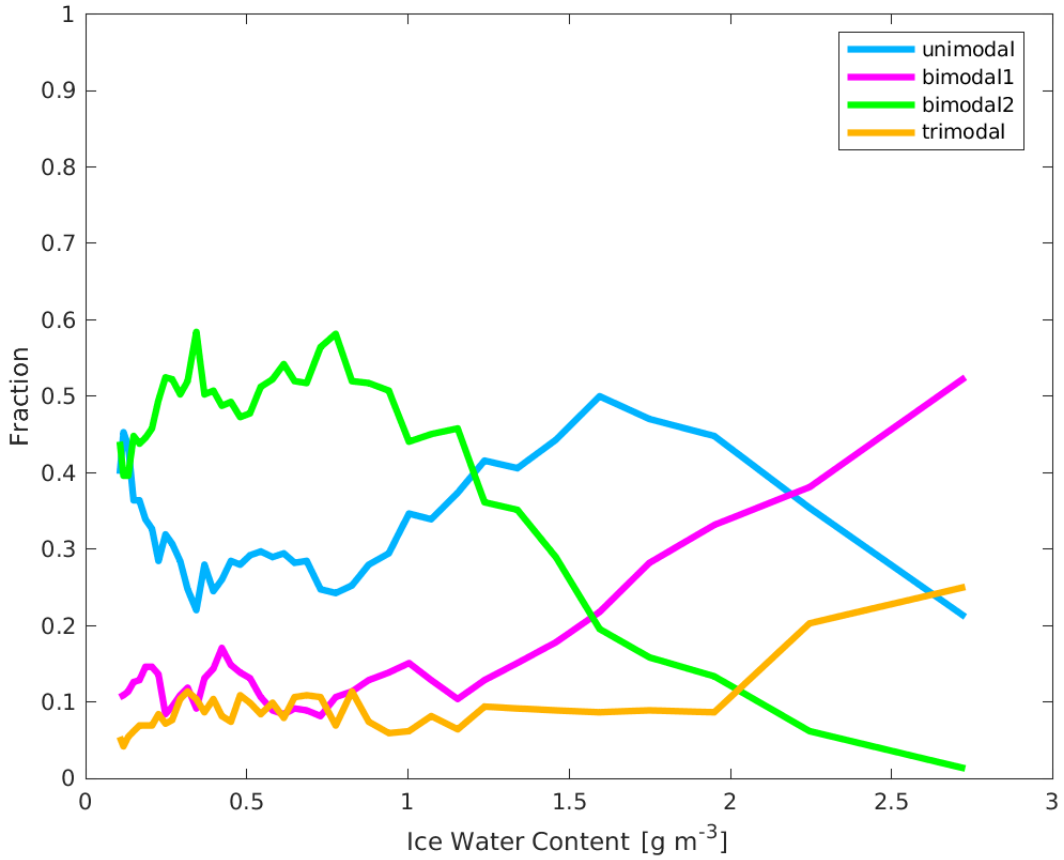


Figure 7: Fraction of PSDs that are unimodal (light blue), bimodal1 (magenta), bimodal2 (green), and trimodal (gold) as a function of ice water content.

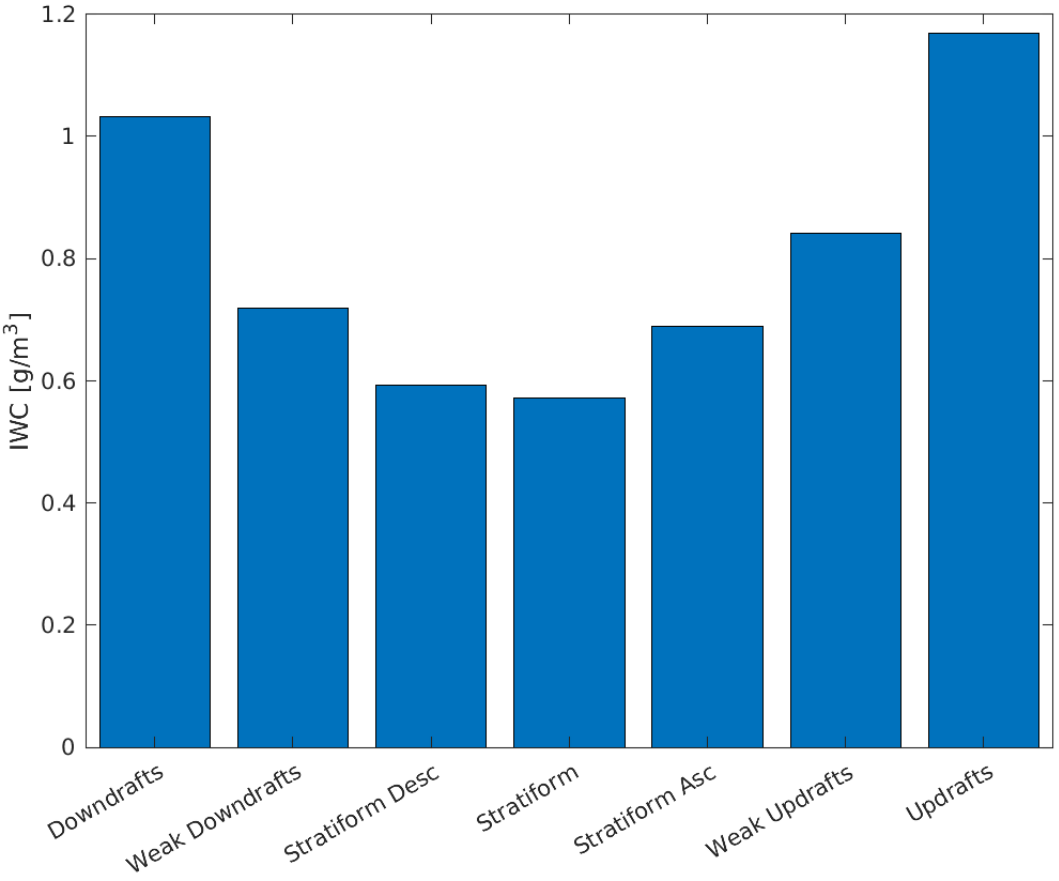


Figure 8: Mean IWC observed by the IKP2 probe as a function of vertical velocity showing IWC increases as updraft and downdraft strength increases.

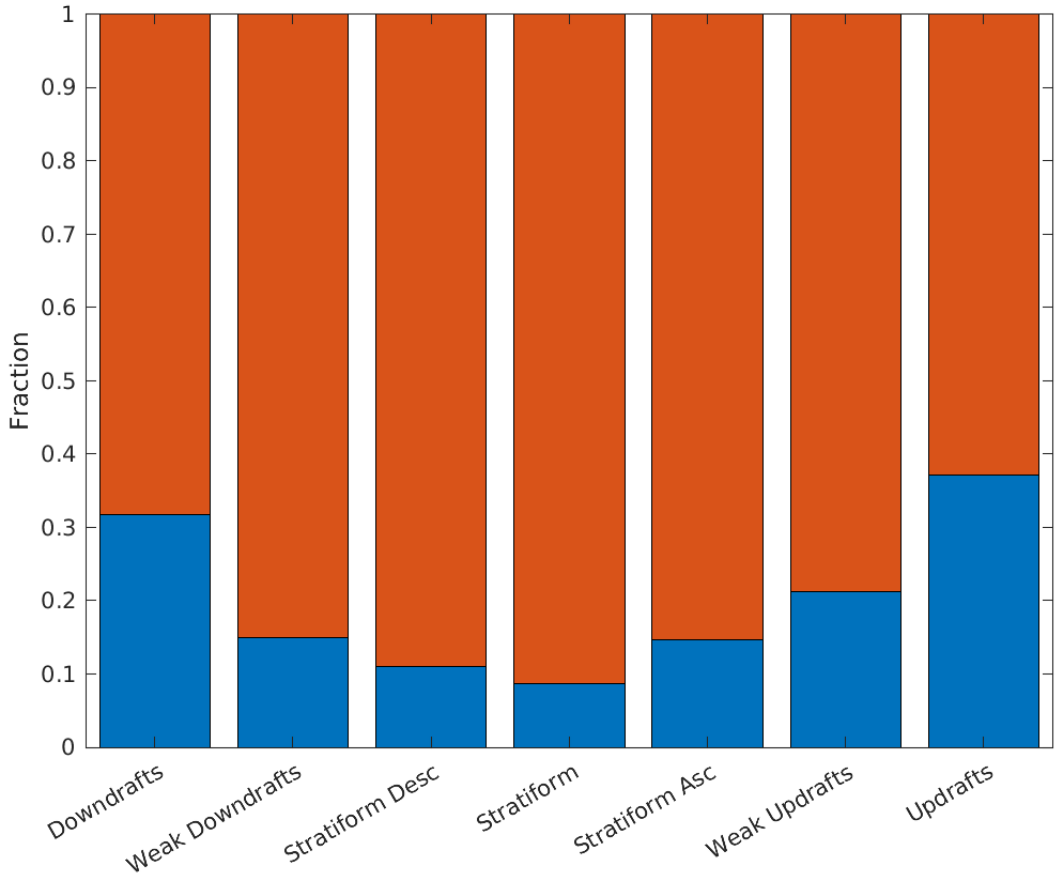


Figure 9: Fraction of PSDs measured at each vertical velocity with IWC ≥ 1.5 g m^{-3} (blue) and with IWC < 1.5 g m^{-3} (orange).

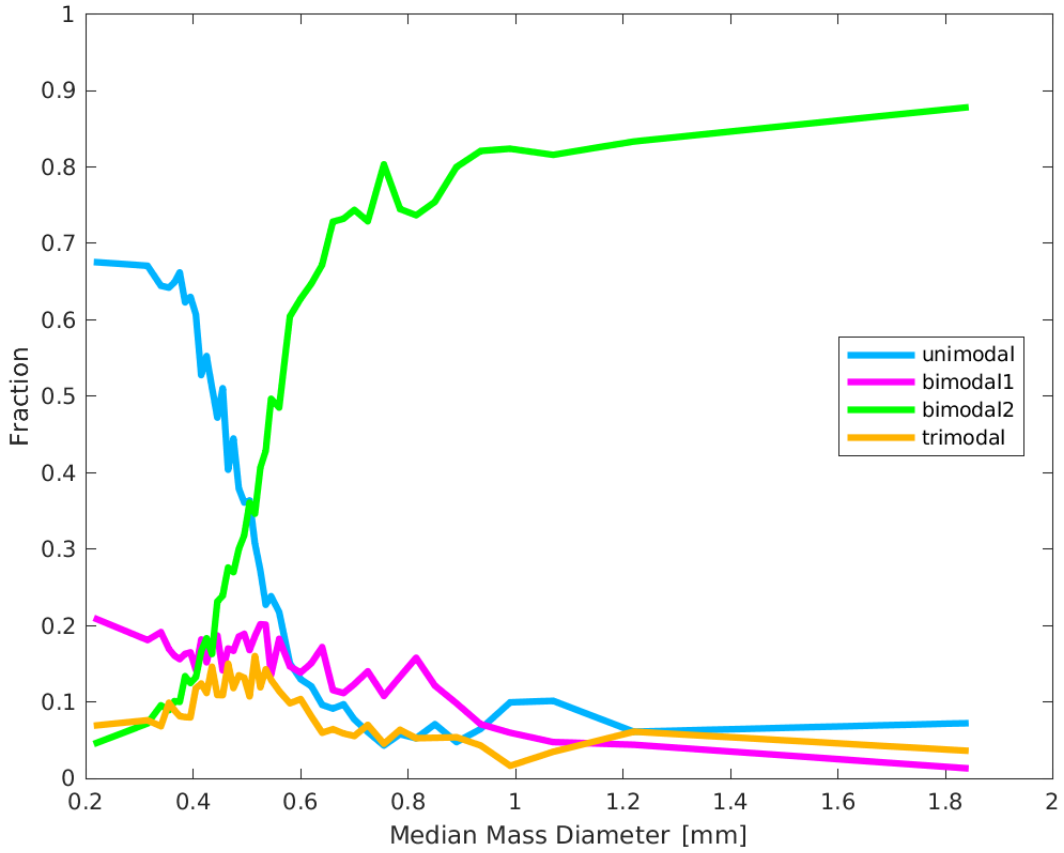


Figure 10: Fraction of PSDs that are unimodal (light blue), bimodal1 (magenta), bimodal2 (green), and trimodal (gold) as a function of median mass diameter.

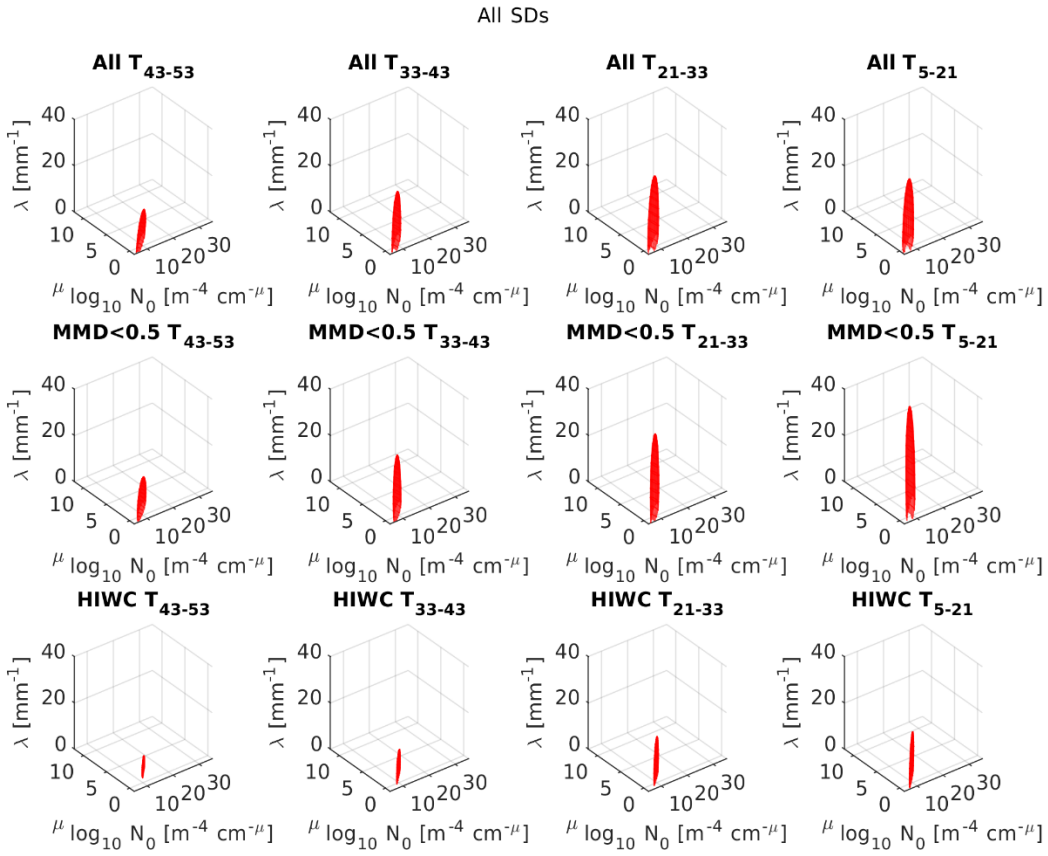


Figure 11: Three-dimensional ellipses of possible N_0, μ, λ values for unimodal distributions in all conditions (top row), small-MMD conditions (middle row), and HIWC conditions (bottom row) near T = -48°C (far left column), T = -38°C (middle left column), T = -27°C (middle right column), and T = -13°C (far right column).

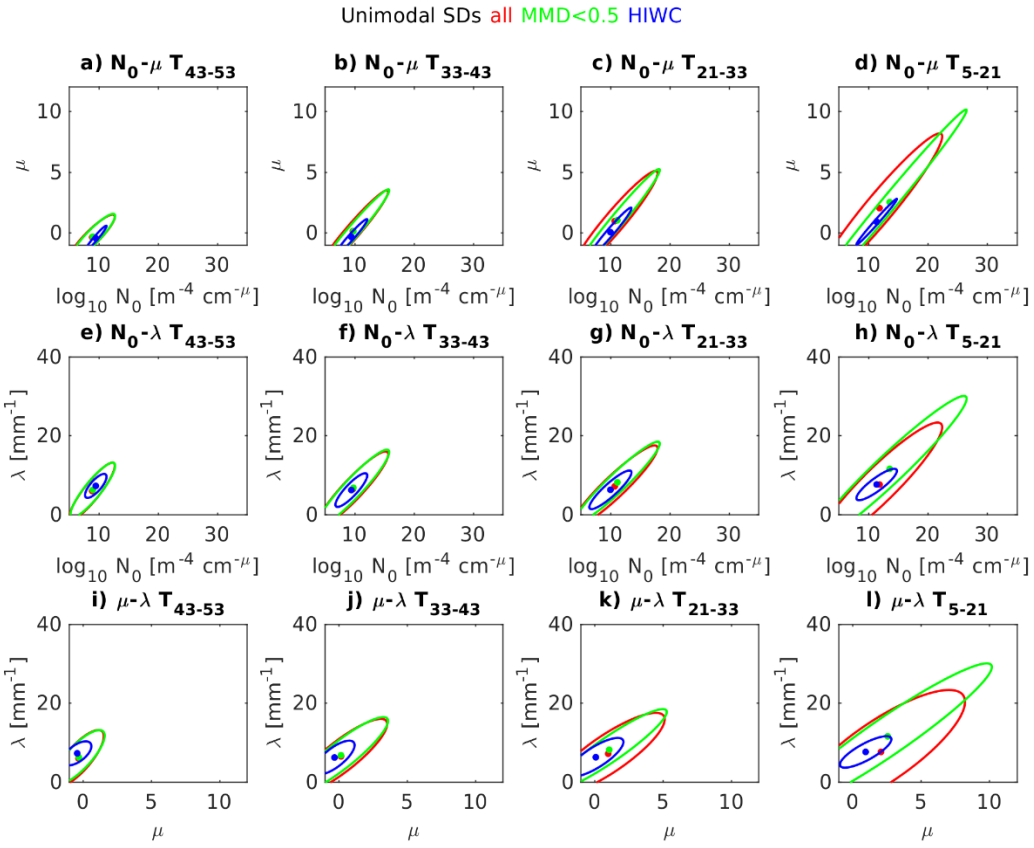


Figure 12: Two-dimensional ellipses of possible (N_0, μ) values (top row), (N_0, λ) values (middle row), and (μ, λ) values (bottom row) for unimodal distributions in all conditions (red), conditions with MMD < 0.5 mm (green), and conditions when HIWCs are present (i.e., MMD < 0.5 mm and IWC > 1.5 g m^{-3}) (blue) near T = -48°C (far left column), T = -38°C (middle left column), T = -27°C (middle right column), and T = -13°C (far right column).

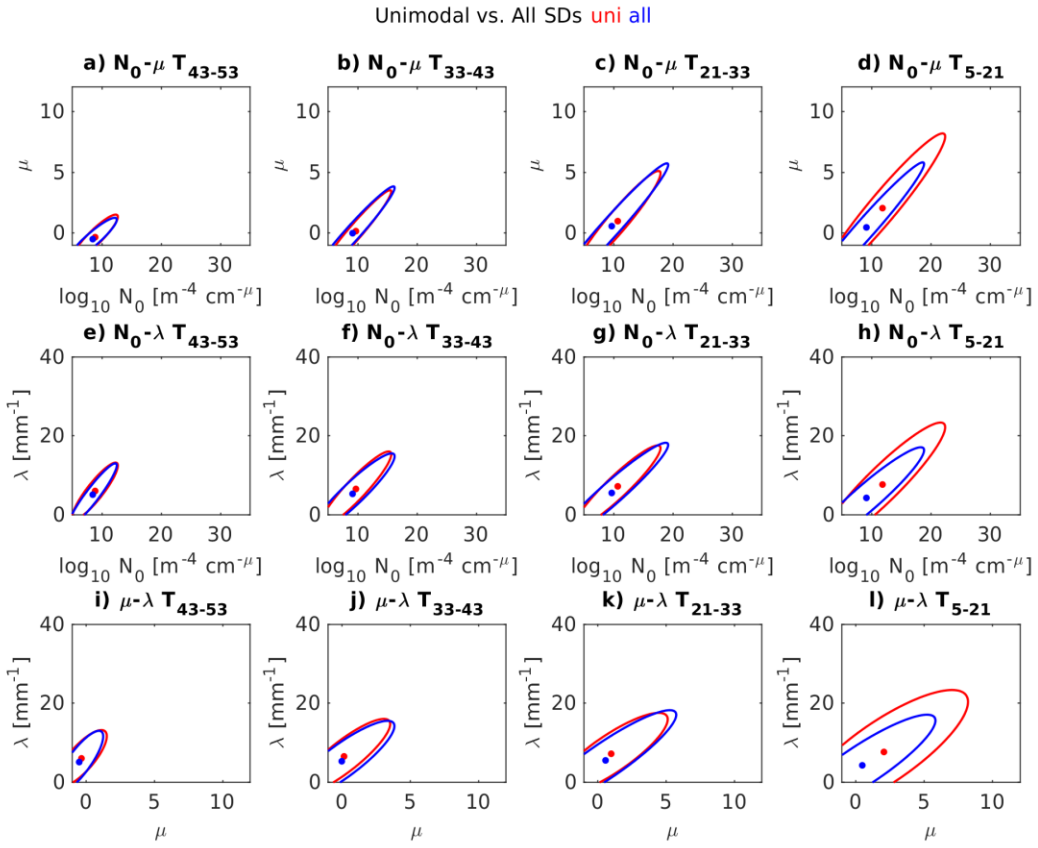


Figure 13: Two-dimensional ellipses of possible (N_0, μ) values (top row), (N_0, λ) values (middle row), and (μ, λ) values (bottom row) for unimodal distributions (red) and for unimodal fits to all distributions (blue) near T = -48°C (far left column), T = -38°C (middle left column), T = -27°C (middle right column), and T = -13°C (far right column).

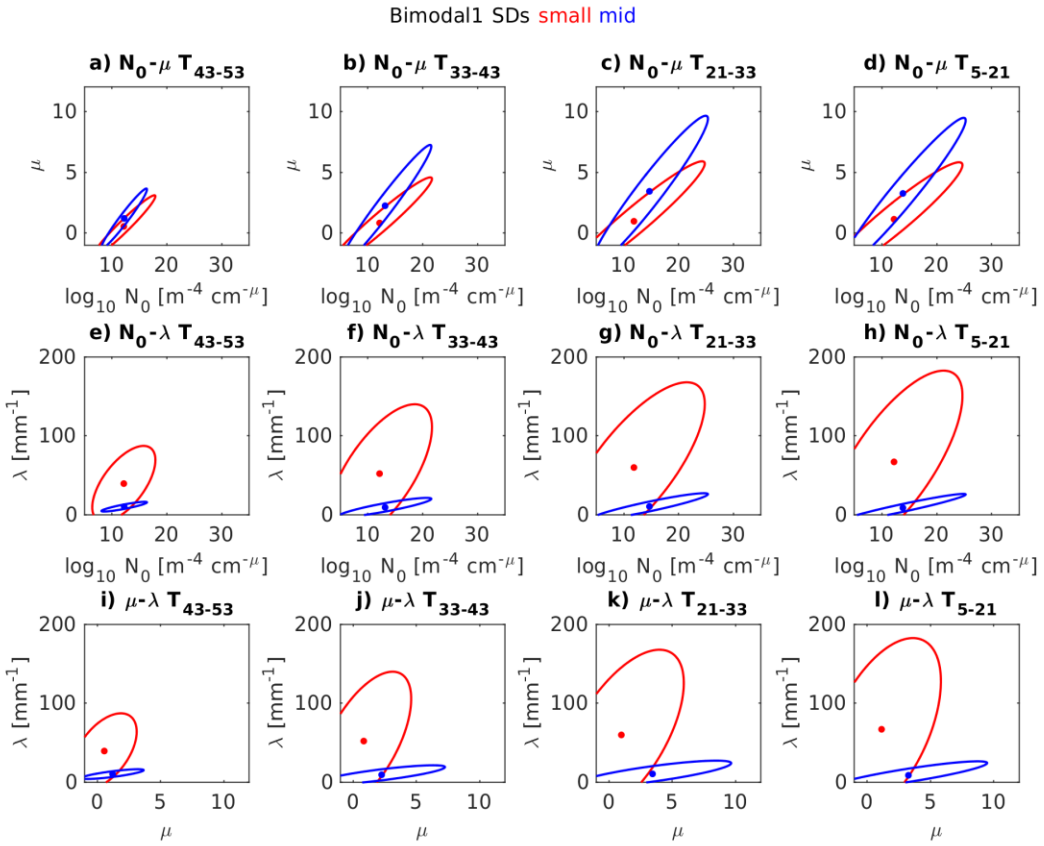


Figure 14: Two-dimensional ellipses of possible (N_0, μ) values (top row), (N_0, λ) values (middle row), and (μ, λ) values (bottom row) for each mode of bimodal1 distributions near T = -48°C (far left), T = -38°C (middle left), T = -27°C (middle right), and T = -13°C (far right). Small mode (red) and middle mode (blue).

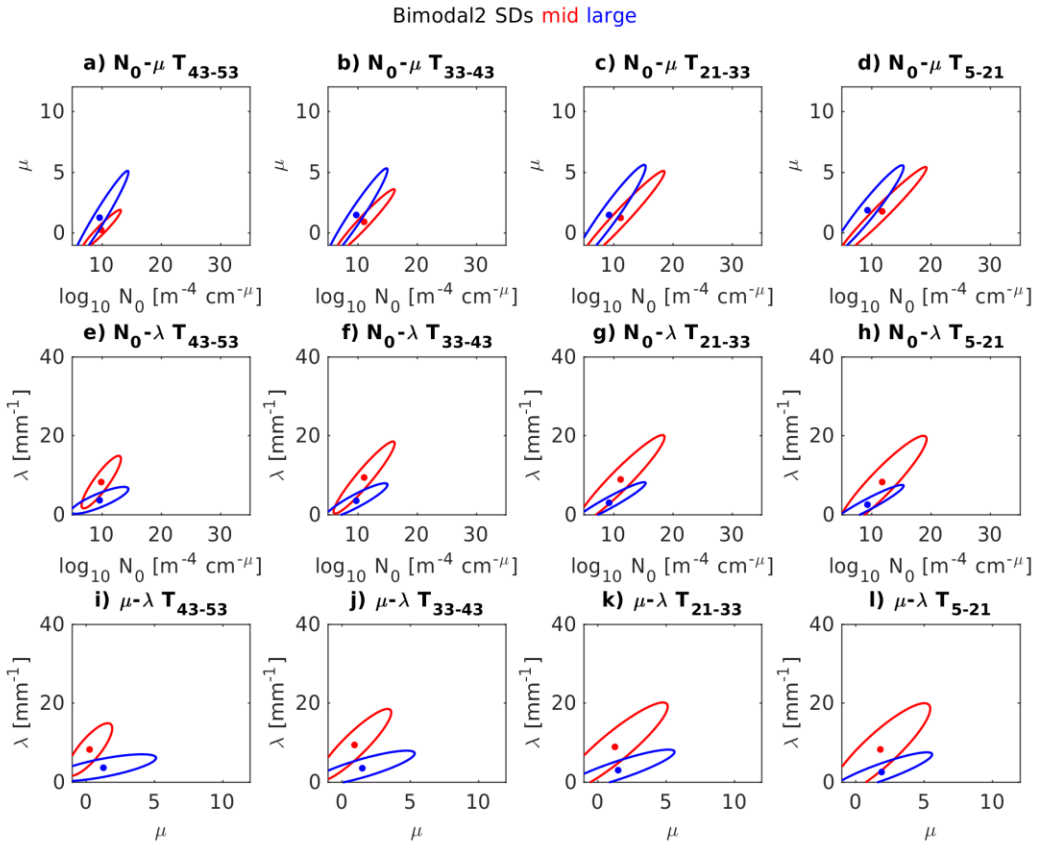


Figure 15: Two-dimensional ellipses of possible (N_0, μ) values (top row), (N_0, λ) values (middle row), and (μ, λ) values (bottom row) for each mode of bimodal2 distributions near T = -48°C (far left), T = -38°C (middle left), T = -27°C (middle right), and T = -13°C (far right). Middle mode (red) and large mode (blue).

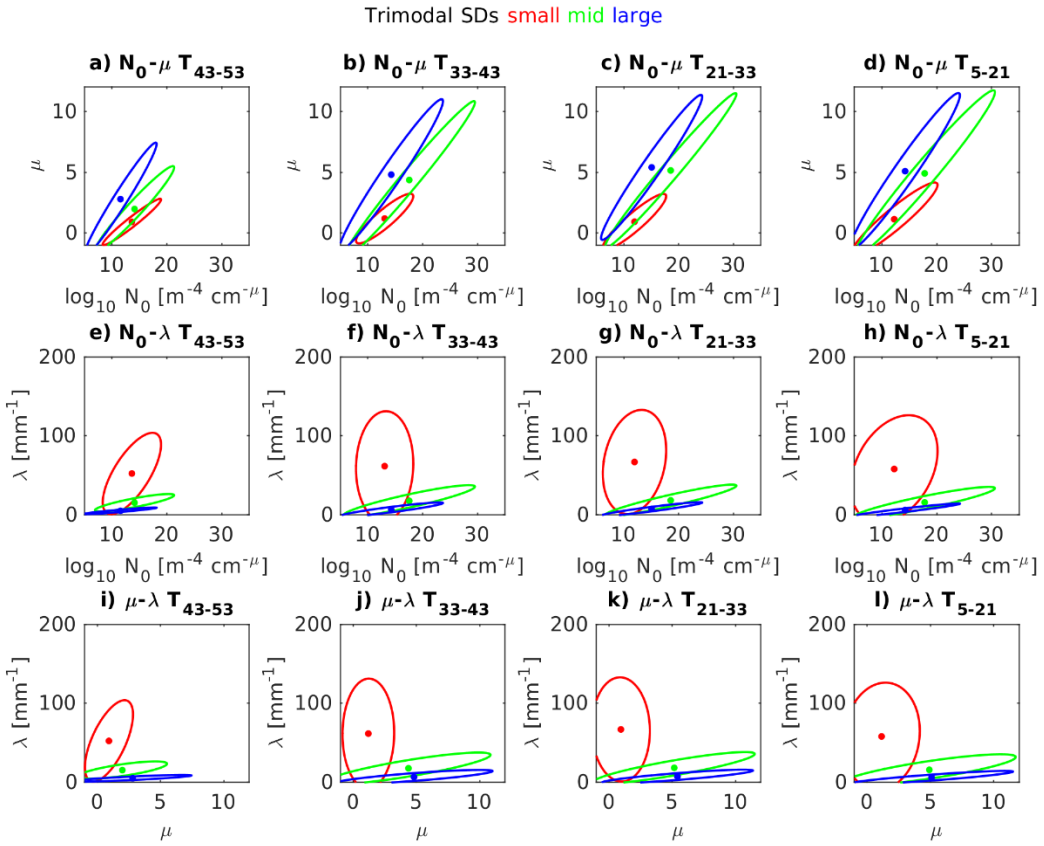


Figure 16: Two-dimensional ellipses of possible (N_0, μ) values (top row), (N_0, λ) values (middle row), and (μ, λ) values (bottom row) for each mode of trimodal distributions near T = -48°C (far left), T = -38°C (middle left), T = -27°C (middle right), and T = -13°C (far right). Small mode (red), middle mode (green), and large mode (blue).

Property	Bias Mean in dBZ (dB)	Bias Standard Deviation in dBZ (dB)	Bias Mean in IWC (g m^{-3})	Bias Standard Deviation in IWC (g m^{-3})	Bias Mean in MMD (μm)	Bias Standard Deviation in MMD (μm)
Unimodal Fit for Unimodal SDs	-0.04	0.22	-0.006 (−0.7%)	0.012 (1.5%)	32 (7.1%)	31 (7.0%)
Bimodal1 Fit	-0.01	0.12	-0.006 (−0.6%)	0.013 (1.2%)	27 (5.1%)	25 (4.8%)
Unimodal Fit for Bimodal1 SDs	-0.08	0.74	-0.006 (−0.6%)	0.013 (1.2%)	9 (1.6%)	44 (8.3%)
Bimodal2 Fit	-0.13	0.22	-0.004 (−0.6%)	0.006 (1.1%)	−2 (−0.3%)	17 (2.3%)
Unimodal Fit for Bimodal2 SDs	-0.66	0.99	0.007 (1.2%)	0.016 (2.7%)	92 (13%)	110 (15%)
Trimodal Fit	-0.06	0.19	-0.006 (−0.6%)	0.017 (1.9%)	8 (1.5%)	14 (2.7%)
Unimodal Fit for Trimodal SDs	-0.25	1.40	-0.004 (−0.4%)	0.032 (3.5%)	99 (19%)	90 (17%)

Table 1: Table of mean and standard deviation of fitting errors in dBZ, IWC, and MMD. Parameters estimated using conversion from concentration to mass used in Leroy et al. (2017).

References

Borovikov, A.M., L.I. Gaivoronskii, E.G. Zak, V.V. Kostarev, I.Z. Mazin, V.E. Minervin, A.Kh. Khrgian, and S.M. Shmeter, 1963: *Cloud Physics.* Israel Program for Scientific Translations, 392 pp.

Bouniol, D., A. Protat, J. Delanoe, J. Pelon, J. Piriou, F. Bouyssel, A.M. Tompkins, D.R. Wilson, Y. Morille, M. Haeffelin, E.J. O'Connor, R.J. Hogan, A.J. Illingworth, D.P. Donovan, and H. Baltink, 2010: Using Continuous Ground-Based Radar and Lidar Measurements for Evaluating the Representation of Clouds in Four Operational Models. *J. Appl. Meteor. Climatol*., **49**, 1971-1991.

Bravin, M., J.W. Strapp, and J. Mason, 2015: An investigation into location and convective lifecycle trends in an ice crystal icing engine database, Tech. rep., SAE Technical Paper 2015-01-2130, *SAE International*, Warrendale, Pennsylvania, USA, doi:10.4271/2015-01-2130.

Connolly, P.J., C. Emersic, and P.R. Field, 2012: A laboratory investigation into the aggregation efficiency of small ice crystals. *Atmos. Chem. Phys.*, **12**, 2055-2076, doi:10.5194/acp-12-2055-2012.

Cooper, W.A., 1986: Ice initiation in natural clouds. *Precipitation Enhancement – A Scientific Challenge, Meteor. Mongr.*, **43**, Amer. Meteor. Soc. 29-32.

Davison, C.R., J. MacLeod, J.W. Strapp, and D. Buttsworth, 2008: Isokinetic total water content probe in a naturally aspirating configuration: Initial aerodynamic design and testing. *Proc. 46th AIAA Aerospace Sciences Meeting and Exhibit*, Reno, NV, American Institute of Aeronautics and Astronautics, AIAA-2008-435. [Available online at http://arc.aiaa.org/doi/abs/10.2514/6.2008-435.]

Davison, C.R., J.W. Strapp, L.E. Lilie, T.P. Ratvasky, and C. Dumont, 2016: Isokinetic TWC evaportator probe: Calculations and systemic error analysis. *Eighth AIAA Atmospheric and Space Environments Conf.*, Washington, D.C., American Institute of Aeronautics and Astronautics, AIAA-2016-4060.

Dezitter, F., A. Grandin, J.L. Brenguier, F. Hervy, H. Schlager, P. Villedieu, and G. Zalamansky, 2013: HAIC (High altitude ice crystals). *Proc. Fifth AIAA Atmospheric and Space Environments Conf.*, San Diego, CA, American Institute of Aeronautics and Astronautics, AIAA-2013-2674. [Available online at http://arc.aiaa.org/doi/abs/20.2514/6.2013-2674.]

Diao, M., M.A. Zondlo, A.J. Heymsfield, S.P. Beaton, and D.C. Rogers, 2013: Evolution of ice crystal regions on the microscale based on in situ observations. *Geophys. Res. Lett.*, **40**, 3473-3478.

Dudhia, J., 1989: Numerical study of convection observed during the Winter Monsoon Experiment using a mesoscale two-dimensional model. *J. Atmos. Sci.*, **46**, 3077-3107, doi:10.1175/1520-0469(1989)046<3077:NSOCOD>2.0.CO;2.

Ferrier, B.S., 1994: A double-moment multiple-phase four-class bulk ice scheme. Part I: Description. *J. Atmos. Sci.*, **51**, 249-280, doi:10.1175/1520-0469(1994)051<0249:ADMMPF>2.0.CO;2.

Field, P.R., R. Wood, P.R.A. Brown, P.H. Kaye, E. Hirst, R. Greenaway, and J.A. Smith, 2003: Ice particle interarrival times measured with a fast FSSP. *J. Atmos. Oceanic Technol.*, **20**, 249-261, doi:10.1175/1520-0426(2003)020<0249:IPITMW>2.0.CO;2.

Field, P.R., A.J. Heymsfield, and A. Bansemer, 2006: Shattering and particle interarrival times measured by optical array probes in ice clouds. *J. Atmos. Oceanic Technol.*, **23**, 1357-1371, doi:10.1175/JTECH1922.1.

Finlon, J.A., G.M. McFarquhar, S.W. Nesbitt, R.M. Rauber, H. Morrison, W. Wu, and P. Zhang, 2019: A novel approach for characterizing the variability in mass-dimension relationships: results from MC3E. *Atmos. Chem. Phys.*, **19**, 3621-3643, doi:10.5194/acp-19-3621-2019.

Fontaine, E., A. Schwarzenboeck, J. Delanoe, W. Wobrock, D. Leroy, R. Dupuy, C. Gourbeyre, and A. Protat, 2014: Constraining mass-diameter relations from hydrometeor images and cloud radar reflectivities in tropical continental and oceanic convective anvils. *Atmos. Chem., Phys*., **14**, 11, 367-11 392.

Fontaine, E., A. Schwarzenboeck, D. Leroy, J. Delanoe, A. Protat, F. Dezitter, J.W. Strapp, and L.E. Lilie, 2020: Statistical analysis of ice microphysical properties in tropical mesoscale convective systems derived from cloud radar and in situ microphysical observations. *Atmos. Chem. Phys*., **20**, 2303-3553. Doi:10.5194/acp-20-3503-2020.

Fridlind, A. A. Ackerman, A. Grandin, F. Dezitter, M. Weber, J. Strapp, A. Korolev, and C. Williams, 2015: High ice water content at low radar reflectivity near deep convection – Part 1: Consistency of in situ and remote-sensing observations with stratiform rain column simulations. *Atmos. Chem. Phys*., **15**, 11713-11728.

Gilmore, M.S., J.M. Straka, and E.N. Rasmussen, 2004: Precipitation uncertainty due to variations in precipitation particle parameters within a simple microphysics scheme. *Mon. Wea. Rev.*, **132**, 2610-2627, doi:10.1175/MWR2810.1.

Heymsfield, A.J. and J.L. Parrish, 1979: Techniques employed in the processing of particle size spectra and state parameter data obtained with the T-28 aircraft platform. NCAR Tech. Note NCAR/TN-137+1A, 77 pp.

Heymsfield, A.J. and C.M.R. Platt, 1984: A parameterization of the particle size spectrum of ice clouds in terms of ambient temperature and the ice water content. *J. Atmos. Sci.*, **41**, 846-855.

Heymsfield, A.J., A. Bansemer, P.R. Field, S.L. Durden, J.L. Stith, J.E. Dye, W. Hall, and C.A. Grainger, 2002: Observations and Parameterizations of Particle Size Distributions in Deep Tropical Cirrus and Stratiform Precipitating Clouds: Results from In Situ Observations in TRMM Field Campaigns. *J. Atmos. Sci*., **59**, 3457-3491.

Heymsfield, A.J., A. Bansemer, C.G. Schmitt, C. Twohy, and M.R. Poellot, 2004: Effective ice particle densities derived from aircraft data. *J. Atmos. Sci*., **61**, 982-1003.

Hoffmann, F., 2020: Effects of entrainment and mixing on the Wegener-Bergeron-Findeisen process. *J. Atmos. Sci.*, **77**, 6, 2279-2296, doi:10.1175/JAS-D-19-0289.1.

Jackson, R.C., G.M. McFarquhar, A. Fridlind, and R. Atlas, 2015: The dependence of cirrus gamma size distributions expressed as volumes in N0-λ-μ phase space and bulk cloud properties on environmental conditions: Results from Small Ice Particles in Cirrus Experiment (SPARTICUS). *J. Geophys. Res. Atmos.*, **120**, 19, 10351-10377, doi:10.1002/2015JD023492.

Korolev. A., 2007: Reconstruction of the sizes of spherical particles from their shadow images. Part I: Theoretical considerations. *J. Atmos. Oceanic Technol.*, **24**, 376-389, doi:10.1175/JTECH1980.1.

Kosarev, A.L. and I.P. Mazin, 1991: An empirical model of the physical structure of upper-layer clouds. *Atmos. Res.*, **26**, 3, 213-228, doi:10.1016/0169-8095(91)90055-2.

Lawson, R.P., L.J. Angus, and A.J. Heymsfield, 1998: Cloud particle measurements in thunderstorm anvils and possible weather threat to aviation. *J. Aircr*., **35**, 113-121, doi:10.2513/2.2268.

Lawson, R.P., D. O'Connor, P. Zmarzly, K. Weaver, B. Baker, Q. Mo, and H. Jonsson, 2006: The 2D-S (Stereo) Probe: Design and Preliminary Tests of a New Airborne, High-Speed, High-Resolution Particle Imaging Probe. *J. Atmos. Oceanic Technol*., **23**, 11, 1462-1477, doi:10.1175/JTECH1927.1.

Lawson, R.P., E. Jenson, D.L. Mitchell, B. Baker, Q. Mo, and B. Pilson, 2010: Microphysical and radiative properties of tropical clouds investigated in TC4 and NAMMA. *J. Geophys. Res*., **115**, D00J08, doi:10.1029/2009JD013017.

Leroy. D., E. Fontaine, A. Schwarzenboeck, and J.W. Strapp, 2016: Ice crystal sizes in high ice water content clouds. Part I: On the computation of median mass diameter from in situ measurements. *J. Atmos. Oceanic Technol.*, **33**, 2461-2476, doi:10.1175/JTECH-D-15-0151.1.

Leroy, D., and Coauthors, 2017: Ice crystal sizes in high ice water content clouds. Part II: Statistics of mass diameter percentiles in tropical convection observed during the HAIC/HIWC project. *J. Atmos. Oceanic Technol.*, **34**, 1, 117-136.

Mason, J.G., J.W. Strapp, and P. Chow, 2006: The ice particle threat to engines in flight. *44th AIAA Aerospace Sciences Meeting*, Reno, Nevada, 9-12 January 2006, AIAA-2006-206.

McFarquhar, G.M., and R. List, 1991: The evolution of three-peak size raindrop distributions in one-dimensional shaft models. Part II: Multiple pulse rain. *J. Atmos. Sci.*, **48**, 1587-1595, doi:10.1175/1520-0469(1991)048<1587:TEOTPR>2.0.CO;2.

McFarquhar, G.M., and A.J. Heymsfield, 1996: Microphysical characteristics of three anvils sampled during the Central Equatorial Pacific Experiment. *J. Atmos. Sci*., **53**, 2401-2423.

McFarquhar, G.M., and A.J. Heymsfield, 1997: Parameterization of tropical cirrus ice crystal size distributions and implications for radiative transfer: results from CEPEX. *J. Atmos. Sci.*, **54**, 17, 2187-2200.

McFarquhar, G.M. and R.A. Black, 2004: Observations of particle size and phase in tropical cyclones: Implications for mesoscale modeling of microphysical processes. *J. Atmos. Sci.*, **61**, 422-439, doi: 10.1175/1520-0469(2004)061<0422:OOPSAP>2.0.CO;2.

McFarquhar, G.M., M.S. Timlin, R.M. Rauber, B.F. Jewett, J.A. Grim, and D.P. Jorgensen, 2007: Vertical variability of cloud hydrometeors in the stratiform region of mesoscale convective systems and bow echoes. *Mon. Wea. Rev.*, **135**, 3405-3428, doi:10.1175/MWR3444.1.

McFarquhar, G.M., T.L. Hsieh, M. Freer, J. Mascio, and B.F. Jewett, 2015: The characterization of ice hydrometeor gamma size distributions as volumes in N0-λ-μ phase space: Implications for microphysical process modeling. *J. Atmos. Sci*., **72**, 2, 892-909, doi:10.1175/JAS-D-14-0011.1.

Meyers, M.P., R.L. Walko, J.Y. Harrington, and W.R. Cotton, 1997: New RAMS cloud microphysics parameterization. Part II. The two-moment scheme. *Atmos. Res.*, **45**, 3-39, doi:10.1016/S0169-8095(97)00018-5.

Milbrandt, J.A., and M.K. Yau, 2005: A multimoment bulk microphysics parameterization. Part I: Analysis of the role of the spectral shape parameter. *J. Atmos. Sci.*, **62**, 3051-3064, doi:10.1175/JAS3534.1.

Mitchell, D.L., 1991: Evolution of snow-size spectra in cyclonic storms. Part II: Deviations from the exponential form. *J. Atmos. Sci.* **48**, 1885-1899, doi:10.1175/1520-0469(1991)048<1885:EOSSSI>2.0.CO;2.

Morrison, H., and A. Gettelman, 2008: A new two-moment bulk stratiform cloud microphysics scheme in the community atmosphere model, version 3 (CAM3). Part I: Description and numerical tests. *J. Climate*, **21**, 15, 3642-3659, doi:10.1175/2008JCLI2105.1.

Morrison, H., G. Thompson, and V. Tatarskii, 2009: Impact of cloud microphysics on the development of trailing stratiform precipitation in a simulated squall line: Comparison of one- and two-moment schemes. *Mon. Wea. Rev.*, **137**, 991-1107, doi:10.1175/2008MWR2556.1.

Protat, A., and Coauthors, 2009: Assessment of Cloudsat reflectivity measurements and ice cloud properties using ground-based and airborne cloud radar observations. *J. Atmos. Oceanic Technol.*, **26**, 1717-1741, doi:10.1175/2009JTECHA1246.1.

Reisner, J., R.M. Rasmussen, and R.T. Bruintjes, 1998: Explicit forecasting of supercooled liquid water in winter storms using the MM5 mesoscale model. *Quart. J. Roy. Meteor. Soc.*, **124**, 1071-1107, doi:10.1002/qj.49712454804.

Rotstayn, L.D., 1997: A physically based scheme for the treatment of stratiform clouds and precipitation in large-scale models. I: Description and evaluation of the microphysical processes. *Quart. J. Roy. Meteor. Soc.*, **123**, 1227-1282, doi:10.1002/qj.49712354106.

Straka, J.M., and E.R. Mansell, 2005: A bulk microphysics parameterization with multiple ice precipitation categories. *J. Appl. Meteor.*, **44**, 445-466, doi:10.1175/JAM2211.1.

Strapp, J.W., A. Korolev, T. Ratvasky, R. Potts, A. Protat, P. May, A. Ackerman, A. Fridlind, P. Minnis, J. Haggerty, J.T. Riley, L.E. Lilie, and G.A. Isaac, 2016a: The High Ice Water Content (HIWC) study of deep convective clouds: Science and technical plan. FAA Rep. DOT/FAa/TC-14/31, 105 pp.

Strapp, J.W., L.E. Lilie, T.P. Ratvasky, C.R. Davison, and C. Dumont, 2016b: Isokinetic TWC evaporator probe: Development of the IKP2 and performance testing for the HAIC-HIWC Darwin 2014 and Cayenne Field Campaigns. *Proc. Eighth AIAA Atmospheric and Space Environments Conf.*, Washington, D.C., American Institute of Aeronautics and Astronautics, AIAA-2016-4059.

Walko, R.L., W.R. Cotton, M.P. Meyers, and J.Y. Harrington, 1995: New RAMS cloud microphysics parameterization. Part I: The single-moment scheme. *Atmos. Res.*, **38**, 29-62, doi:10.1016/0169-8095(94)00087-T.

Willis, P.T., 1984: Functional fits of observed drop-size distributions and parameterization of rain. *J. Atmos. Sci.*, **41**, 1648-1661.

Zhao, Y., G.G. Mace, and J.M. Comstock, 2010: The occurrence of particle size distribution bimodality in midlatitude cirrus from ground-based remote sensing data. *J. Atmos. Sci.*, **68**, 1162-1167, doi:10.1175/2010JAS3354.1.